Research Paper

EERI EARTHQUAKE SPECTRA

Earthquake Spectra
1–32

DOI: 10.1177/8755293020911134
journals.sagepub.com/home/eqs
SAGE

Simulation and analysis of a vertically irregular building subjected to near-fault ground motions

Jui-Liang Lin, Wen-Hui Chen, Fu-Pei Hsiao, Yuan-Tao Weng, Wen-Cheng Shen, Pu-Wen Weng, Yi-An Li, and Shu-Hsien Chao

Abstract

A shaking table test of a three-story reinforced concrete (RC) building was conducted. The tested building is vertically irregular because of the first story's elevated height and the third story's added RC walls. In addition to far-field ground motions, near-fault ground motions were exerted on this building. A numerical model of the three-story building was constructed. Comparing with the test results indicates that the numerical model is satisfactory for simulating the seismic response of the three-story building. This validated numerical model was then further applied to look into two issues: the effective section rigidities of RC members and the effects of near-fault ground motions. The study results show the magnitude of the possible discrepancy between the actual seismic response and the estimated seismic response, when the effective section rigidities of the RC members are treated as in common practice. An incremental dynamic analysis of the three-story RC building subjected to one far-field and one near-fault ground motion, denoted as CHY047 and TCU052, respectively, was conducted. In comparison with the far-field ground motion, the near-fault ground motion is more destructive to this building. In addition, the effect of the selected near-fault ground motion (i.e. TCU052) on the building's collapse is clearly identified.

Keywords

Vertically irregular building, near-fault ground motion, shaking table test, reinforced concrete building, numerical model, effective section rigidity, incremental dynamic analysis, building collapse

Date received: 8 July 2018; accepted: 1 February 2020

National Center for Research on Earthquake Engineering, Taipei, Taiwan

Corresponding author:
Jui-Liang Lin, National Center for Research on Earthquake Engineering, 200, Section 3, Xinhai Rd., Taipei 106, Taiwan, R.O.C.
Email: jllin@ncree.narl.org.tw

Introduction

Buildings where the first stories are used as shopping stores or parking lots and where the other stories are used as residences are very common in many places around the world. Due to such different functionalities, the first story usually has an elevated story height and less partition walls in comparison with the other stories. This phenomenon very likely yields vertical irregularity. One collapsed building, which caused 115 fatalities during the Meinong earthquake on 6 February 2016 in southern Taiwan, was of this building type. Several buildings, damaged in the same seismic event but resulting in much fewer casualties, also had the same type of vertical irregularity (Chiou et al., 2018). In addition, because there are many active faults close to the populated cities in Taiwan, the effect of near-fault ground motions on the seismic demands of vertically irregular buildings is a critical issue, and particularly needs thoughtful address in Taiwan.

The complex behavior of vertically irregular buildings has attracted a significant amount of research (Soni and Mistry, 2006). Moehle and Alarcon (1986) conducted shaking table tests for wall-frame structures with irregular vertical configurations. They concluded that dynamic method was capable of estimating the peak displacement responses, whereas static method was failed in this purpose. Valmundsson and Nau (1997) suggested that as long as the strength of the first story is less than that of its second story, which was stricter than the code stipulation (Uniform Building Code (UBC), 1994), the building should be treated as a vertically irregular building. Michalis et al. (2006) pointed out that strength irregularity poses more significant influence on seismic responses of buildings, compared with stiffness irregularity. In addition, among strength, stiffness, and mass irregularities, mass irregularity has the least influence on seismic responses. Chintanapakdee and Chopra (2004) evaluated the accuracy of using modal pushover analysis (MPA) method (Chopra and Goel, 2002) for the seismic analysis of vertically irregular buildings. They concluded that the MPA method is not suitable for buildings with a strong or stiff-and-strong first story/lower half. Note that the abovementioned literatures, studies associated with vertically irregular buildings, appeared not explicitly addressing the effects of near-fault ground motions on seismic responses of buildings.

On the aspect of near-fault ground motions, Alavi and Krawinkler (2004) pointed out that there are strong velocity pulses in the forward direction of near-fault ground motions, which cause more drastic seismic demands in comparison with far-field ground motions. In addition, when the vibration period of a building is greater than the period of the velocity pulse, the upper stories of the building will yield earlier than lower stories. In contrast, when the vibration period of a building is less than the period of the velocity pulse, the maximum ductility demand always occurs at lower stories (Alavi and Krawinkler, 2004). Chopra and Chintanapakdee (2001) studied the seismic responses of single-degree-of-freedom (SDOF) systems subjected to far-field and near-fault ground motions. They pointed out that while setting the ductility demands being identical, the strength demands of SDOF systems subjected to near-fault ground motions are greater than those subjected to far-field ground motions. In order to predict the distinct type of inelastic demand caused by near-fault ground motions, Baltzopoulos et al. (2016) proposed specific oscillators with trilinear backbone curves. In comparison with far-field ground motions, these researches (Alavi and Krawinkler, 2004; Baltzopoulos et al., 2016; Chopra and Chintanapakdee, 2001) consistently showed the distinct seismic demands of structures subjected to near-fault ground motions.

In light of the prevalence of vertically irregular buildings and the distinctiveness of seismic demands caused by near-fault ground motions, it is desirable to study the seismic

(a) (b)

Figure 1. (a) NCREE Tainan lab and (b) The 8 m × 8 m shaking table and the three-story RC building (the white part).

Table 1. Specifications of the 8 m × 8 m shaking table

	Horizontal axis	Vertical axis
Stroke	± 1.0 m	± 0.40 m
Velocity	± 2.0 m/s	± 1.0 m/s
Acceleration	±0.75 g (250 ton)	±0.5 g (250 ton)
	±1.4 g (100 ton)	±0.8 g (100 ton)
	±2.5 g (bare table)	±3.0 g (bare table)
Overturning moment	500 ton-m (bi-axial)	
	1000 ton-m (uni-axial)	
Weight of table	68.2 ton	
Reaction mass	3992 ton	

responses of vertically irregular buildings subjected to near-fault ground motions. Nevertheless, such studies, especially those through conducting shaking table tests, seem comparatively rare. This may be because the shaking tables capable of reproducing near-fault ground motions, which are usually with the characteristics of large displacements and strong velocity pulses, are not commonly accessible across the world. With the aim of addressing the issue of near-fault ground motions, Taiwan's National Center for Research on Earthquake Engineering (NCREE) unveiled its Tainan lab (Figure 1a) on 9 August 2017. At the NCREE Tainan lab, an 8 m × 8 m 6 degree-of-freedom tri-axial shaking table (Figure 1b) with a 250 ton payload was established to simulate near-fault ground motions. The specifications of the shaking table (Table 1) indicate that the shaking table is capable of high velocities and long strokes, which are necessary for reproducing near-fault ground motions. On the opening date of the NCREE Tainan lab, the brand-new shaking table publicly performed its debut through the shaking of a three-story reinforced concrete (RC) building (Figure 1b). The three-story RC building is vertically irregular because of its elevated first story and the RC walls infilled only on the third story. This three-story RC building is an intended reflection of the type of buildings collapsed during the aforementioned Meinong earthquake in 2016. This study calibrates a numerical model to simulate the dynamic responses of the three-story RC building obtained from the shaking table test. The satisfactory simulation results provide insights into the modeling of RC structures. Through this validated numerical model, this study further analyzes the three-story RC building subjected to various intensities of one near-fault and one far-field ground motion. The analytical results are examined to characterize the effects of the selected near-fault ground motion on this vertically irregular building. This study may serve as a bridge between analytical and experimental studies of vertically irregular buildings shaken by near-fault ground motions.

Experimental description

A shaking table test was conducted, in addition to a material test and component test, both of which are useful for the prediction of the dynamic responses of the test model. The experimental details are described in this section.

Test model

The three-story RC building was used as the test model, approximated as a 1/2-scaled model of an actual building constructed in 1995 and damaged in the 2016 Meinong earthquake. The numbers of stories and bays of the actual building are greater than those of the three-story building test model; however, the member sizes and arrangements of reinforcements of the three-story building were scaled from those of the actual building, which was designed according to Taiwan Building Technical Regulations (Construction and Planning Agency, Ministry of the Interior (CPAMI), 1989). In order to protect the shaking table, a steel frame (the dark-red part shown in Figure 1b) was erected as a safety device that could be leaned upon by the building when unexpected collapse occurs. Figure 2a to c show the top view, front elevation, and side elevation of the three-story building, respectively. There are one bay and two bays in the x- and y-directions of the three-story building, respectively. Each bay is 350 cm. The walls are infilled only on the two outsides of the third story along the x-direction (Figure 2c). The first story height, measured from the top of the pedestals (i.e. footings) to the top of the first floor slab, is 300 cm. Both the second and third story heights, measured from slab top to slab top, are 150 cm (Figure 2b and c). The beam size is 25 cm $\times$ 40 cm for all beams. The size of the three columns in column line A, denoted as C2, is 75 cm $\times$ 30 cm, and the size of the three columns in column line B, denoted as C1, is 30 cm $\times$ 30 cm (Figure 2a). Figure 2d and e show the details of the reinforcements for beams and columns. The materials used for #3 (i.e. 10ϕ) and #6 (i.e. 19ϕ) reinforcements are SD280W and SD420W, respectively. That is to say, the nominal yielding strengths of #3 (i.e. 10ϕ) and #6 (i.e. 19ϕ) reinforcements are 280 and 420 MPa, respectively. The designed concrete's 28-day compression strength, denoted as f_c' is 21 MPa. The thickness of the slabs and walls are 10 cm and 15 cm, respectively. Both the details of the reinforcements for walls and slabs are #3@15 cm on two sides and in two directions. The size of each concrete pedestal is 75 cm (L) $\times$ 115 cm (W) $\times$ 70 cm (H). The pedestal is connected with a steel base plate through shear studs. The base plates are fixed onto the shaking table through bolts (Figure 2f). Two additional concrete mass blocks, each of which is 110 cm (L) $\times$ 110 cm (W) $\times$ 50 cm (H), are embedded in the slabs of each of the second and the third stories (Figure 2a). Because the 50 cm height of the mass blocks is greater than the slab's thickness (i.e. 10 cm), the 30 cm and 10 cm heights of the mass blocks protrude from the bottom and top surfaces of the slabs, respectively. The resultant weight of the three-story building, excluding the safety device, is 505 kN, which consists of 183.8, 168.9, and 152.3 kN for the first, second, and third stories, respectively.

It is worth noting that a modularized construction method was applied to this three-story building, using a combination of modules A and C (Figure 2g) connected via steel connection plates (Figure 2 h). The vertical bars of the columns and walls are welded to

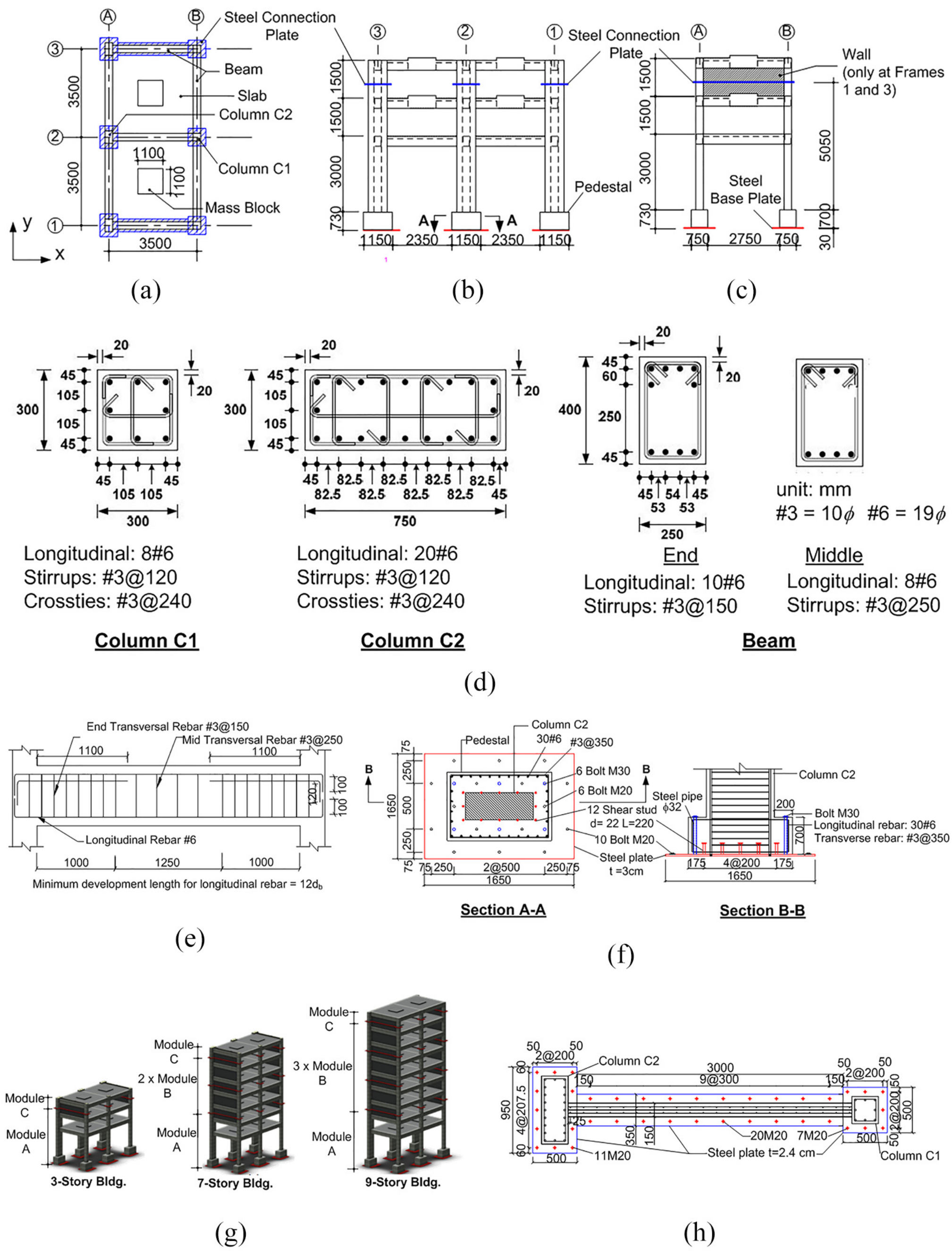

Figure 2. (a) The top view, (b) the front elevation, and (c) the side elevation of the three-story building; (d) the cross sections of beams and columns; (e) the reinforcements along beam length; (f) the detail of the pedestal; (g) the modular design of buildings; (h) the detail of the steel connection plate.

the steel connection plates. Consecutive modules are connected by having their respective steel plates bolted together (Figure 2g and h). The concrete for different modules can be simultaneously poured and cured on the ground, prior to module assembly, thus

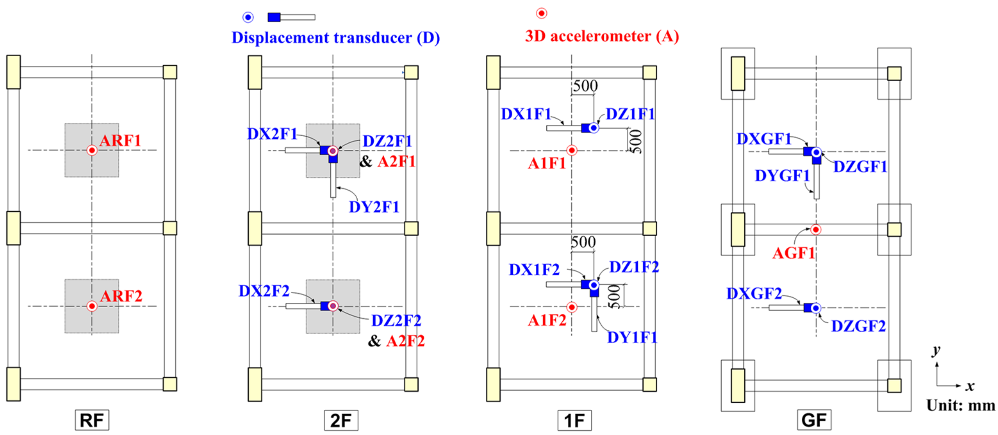

Figure 3. The layout of accelerometers and displacement transducers.

shortening the construction period. In addition, the intact modules of a building, after the shaking table tests, can be used again in other buildings. Furthermore, the erection of the buildings on the shaking table is not limited by the load capacity of the overhead crane in the laboratory. Therefore, this modularized construction allows buildings with different numbers of stories (Figure 2g) to be efficiently and economically constructed and tested in the laboratory.

Instrumentation

Three-direction accelerometers (abbreviated as "A") were installed on the ground floor (i.e. the top surface of the shaking table), as well as the first, second, and third floors to measure the floor accelerations in the three directions (i.e. x-, y-, and z-directions). In addition, displacement transducers (abbreviated as "D") were installed on the ground floor, first, and second floors to measure the inter-story displacements in the x- and y-directions. The layout of the accelerometers and displacement transducers is shown in Figure 3. "X" and "Y" in Figure 3 are the measurement directions of the displacement transducers. "RF", "2F", "1F", and "GF" denote the floor number on which the instruments are located. The last digit on the instrument tag, that is, "1" or "2," differentiates the locations of instruments installed on the same floor.

Material test

Before performing the shaking table test, material tests and component tests were conducted. The tension tests of the reinforcements showed that the yielding strengths of the #3 and #6 reinforcements are 355 MPa and 454 MPa, respectively. The compression tests of the three concrete cylinders showed that the average f_c' is 21.96 MPa.

Component test

Static cyclic tests of the single columns C1 and C2 were used as the component test. The component test was conducted using the multi-axial testing system (MATS) at NCREE's Taipei lab. The MATS (Figure 4a) has 6 degrees of freedom, and can apply a combination

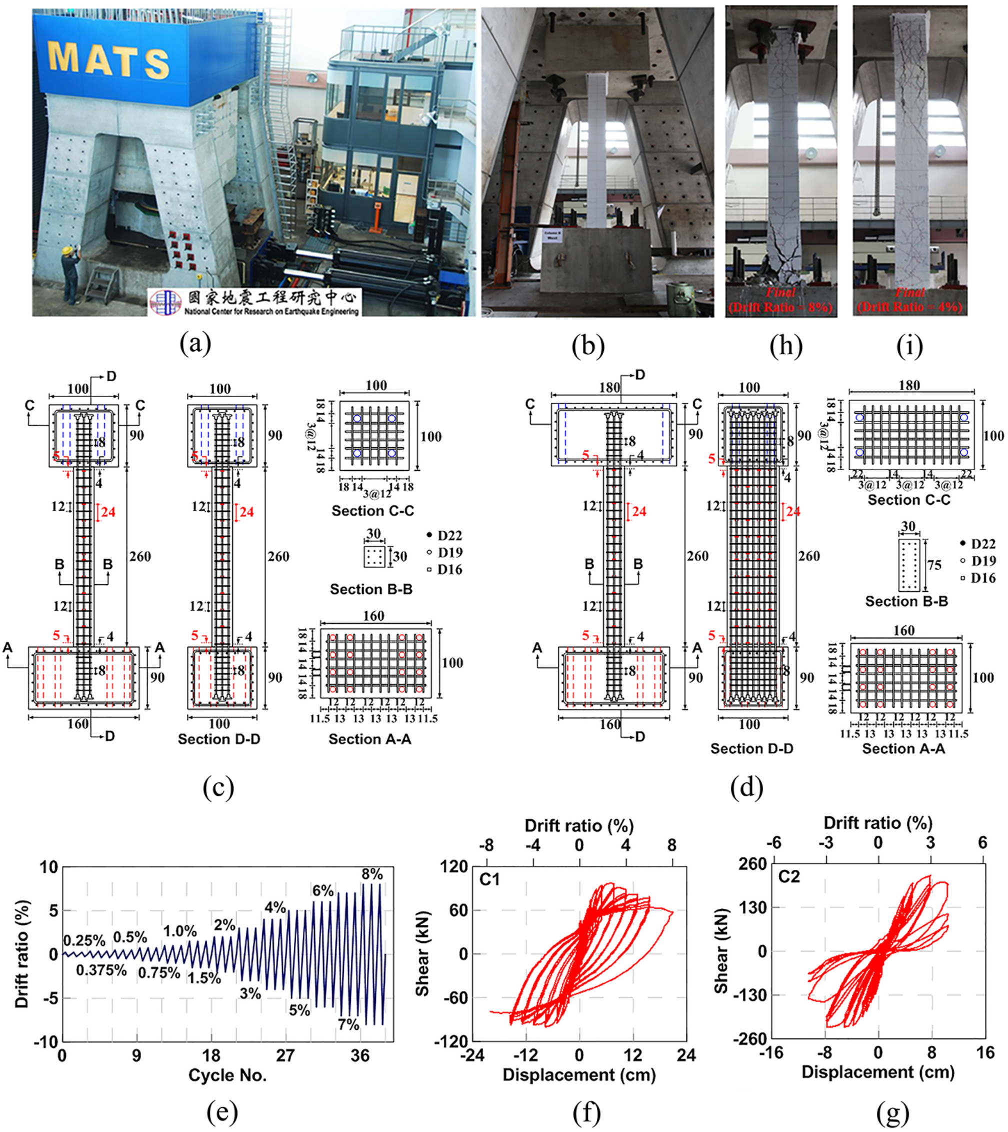

Figure 4. (a) The multi-axial testing system (MATS), (b) specimen C2 installed in the MATS; the design drawings of specimens (c) C1 and (d) C2, (e) the drift history of the static cyclic tests; the hysteresis loops of columns (f) C1 and (g) C2, and the state of damage of specimens (h) C1 and (i) C2 at the end of their static cyclic tests.

of vertical, lateral, and transverse loading, and moments in three directions on a specimen. Figure 4b shows C2 installed in the MATS. Figure 4c and d denote the design drawings for C1 and C2, respectively, each of which contains the column itself and the top and bottom fixing blocks. The clear height of the columns C1 and C2 is 260 cm, which is equal to that of the first story's columns, measured from the top of the pedestals to the bottom of the beams. A fixed–fixed boundary condition was used at the two ends of the columns C1 and C2.

Figure 4e shows the drift history of the static cyclic tests of specimens C1 and C2. There are 13 peak drift ratios, ranging from 0.25% to 8.0%, each of which is repeated for three cycles (Figure 4e). Constant axial loads equal to $0.12A_gf_c$' and $0.06A_gf_c$' were applied to columns C1 and C2, respectively, where A_g is the cross-sectional area of the columns. Figure 4f and g show the hysteresis loops of columns C1 and C2, respectively. Figure 4f indicates that column C1 has a stable hysteresis loop. Nevertheless, the hysteresis loop for column C2 has a significant pinch phenomenon accompanied by a significant drop of strength at a drift ratio of 4% (Figure 4g). Figure 4h and i show photos of the specimens C1 and C2 at the end of their static cyclic tests, that is, at drift ratios of 8% and 4%, respectively. Figure 4h shows that a plastic hinge formed at the bottom end of column C1. Figure 4i shows a substantial vertical split from the top of column C2 to the middle of the specimen. This vertical split caused the significant drop of strength of column C2 at the 4% drift ratio (Figure 4g).

Shaking table test

The ground motion records of the 1999 Chi-Chi earthquake recorded at the TCU052 and CHY047 stations, denoted as TCU052 and CHY047, respectively, were selected to shake the building. TCU052 and CHY047 were a near-fault ground motion record and a far-field ground motion record, respectively. The two components of TCU052 and CHY047 were scaled and applied in the x- and z- (i.e. vertical) directions of the building. Table 2 shows the input sequence of the scaled ground motion records. The amplitudes of the selected ground motion records were scaled so that the x-directional peak ground acceleration (PGA) equals the target values (Table 2), while keeping the frequency contents unchanged. The target values of the PGA do not represent the code-specified design hazard levels for Taiwan. In fact, besides ensuring that the building remains intact during the tests before the grand opening, the PGA target values were selected with the aim of ensuring the building's excursion significantly beyond its elastic limit but no collapse occurred during the tests on the date of the grand opening. In addition, because the three-story building is a 1/2-scaled model, the time scales of all the original ground motion records were modified by dividing by $\sqrt{2}$ according to the theory of dimensional analysis (Gibbings, 2011). Figure 5a and b show the x- and z-directional accelerations measured on the top surface of the shaking table, while applying CHY047 scaled to the x-directional PGA equal to 420 cm/s^2. Figure 5c and d show the x- and z-directional accelerations measured on the top surface of the shaking table, while applying TCU052 scaled to the x-directional PGA equal to 1000 cm/s^2. It is noted that the measured x-directional PGA shown in Figure 5c is not equal to the expected value, 1000 cm/s^2. This obvious discrepancy was due to the lack of experience in using the sophisticated control of the new shaking table for reproducing near-fault ground motions. Figure 5e and f show the $\xi = 5\%$

Table 2. The input sequence of the scaled ground motion records

Date of test	Ground motion record	Target value of the x-directional PGA (cm/s^2)	Note
28 July 2017	TCU052	350	Elastic-level shakings
	CHY047	420	
9 August 2017	TCU052	800	Inelastic-level shakings
	TCU052	1000	

PGA: peak ground acceleration.

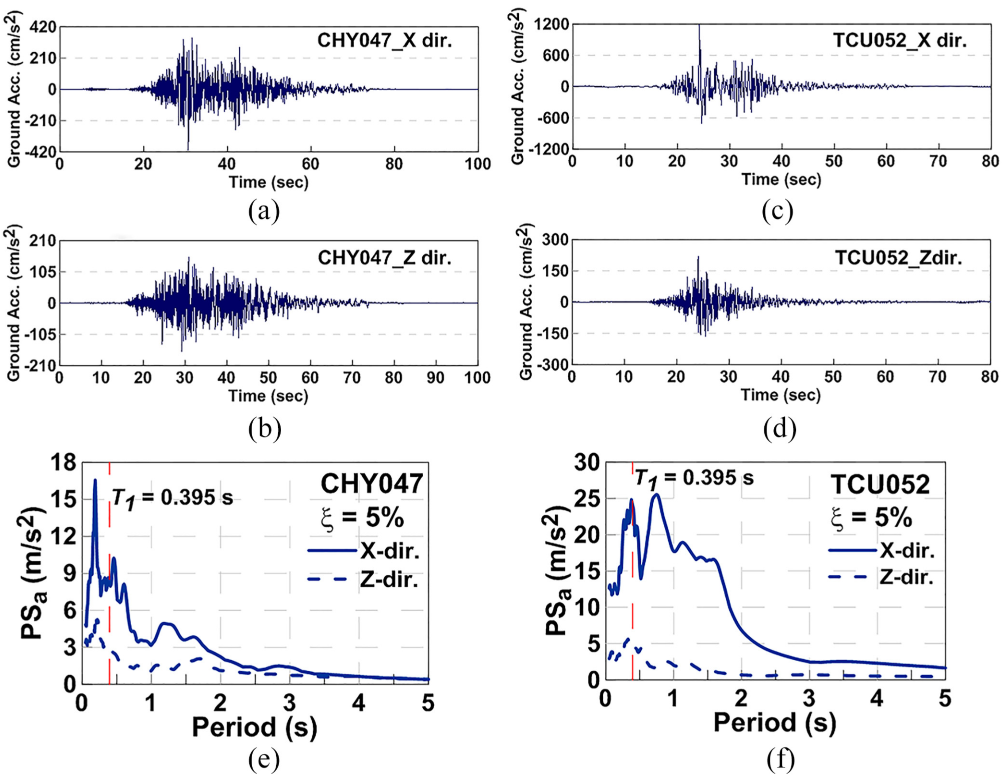

Figure 5. The measured acceleration records on the shaking table's top surface: (a) and (b) are CHY047 scaled to the x-directional PGA = 420 cm/s^2; (c) and (d) are TCU052 scaled to the x-directional PGA = 1000 cm/s^2; the ξ = 5% damped pseudo-acceleration spectra of the measured (e) CHY047 and (f) TCU052.

damped pseudo-acceleration spectra of the measured CHY047 (Figure 5a and b) and TCU052 (Figure 5c and d), respectively.

At the end of the TCU052 shaking, obvious horizontal cracks were observed in columns C1 (Figure 6a) and C2 (Figure 6b). The beam-column joints also had diagonal cracks (Figure 6a and b). In comparison with the cracks in columns C1 and C2, the vertical cracks at the two ends of the x-directional beams appeared to be minor (Figure 6c). In addition, the cracks at the end of the beam connecting to column C2 (i.e. the right end of the beam shown in Figure 6c) were more significant than those at the end of the beam connecting to column C1 (i.e. the left end of the beam shown in Figure 6c). The measured seismic responses including the roof accelerations, roof displacements, and the inter-story drifts are illustrated in the next section, and compared with those obtained from the numerical model.

Numerical simulation

Numerical model

The simulated seismic responses were obtained from the nonlinear response history analyses by means of the PISA3D structural analysis program (Lin et al., 2009). The numerical

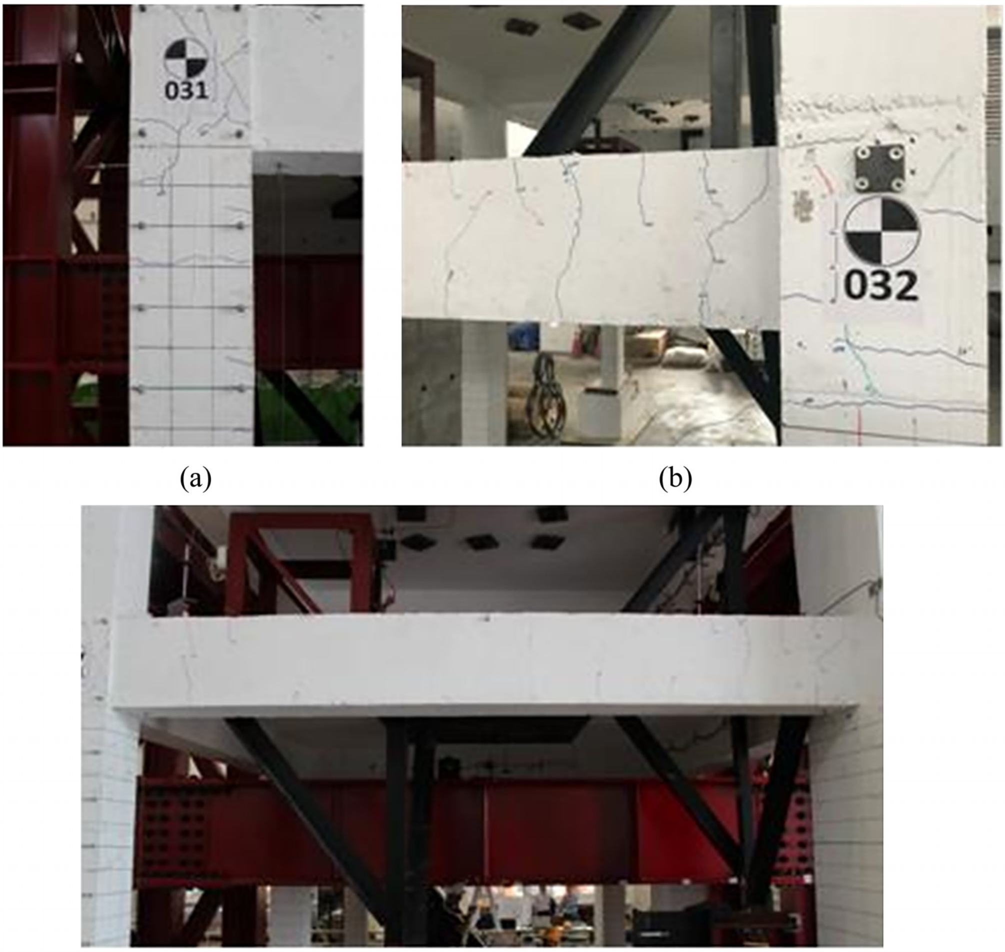

(a) (b)

(c)

Figure 6. The damage states of the columns (a) C1 and (b) C2, and (c) the x-directional beam on the first story at the end of the TCU052 shaking.

model of the building consists of beam-column elements and panel elements for simulating beams/columns and RC walls, respectively. The beam-column element is an elastic component connected with two different types of plastic hinges (shear and flexure) in series at each end, as shown in Figure 7a. Thus, rather than using the fiber beam-column element (Spacone et al., 1996), the beam-column element with lumped plasticity at the two ends of the element is adopted in the numerical model. In this element, a constant section with its material and section properties (e.g. moment of inertia, and section modulus, etc.) are defined (Lin et al., 2009). The flexibility matrix of a beam-column element is the sum of the flexibility matrices of the elastic portion and the lumped-plasticity portion. The stiffness matrix of a beam-column element is then computed as the inverse of its corresponding flexibility matrix. The flexibility of the lumped-plasticity portion varies according to the state of the adopted material model, whereas the flexibility of the elastic portion of the element remains constant (Lin et al., 2009; Tsai and Lin, 2003). The panel element has five

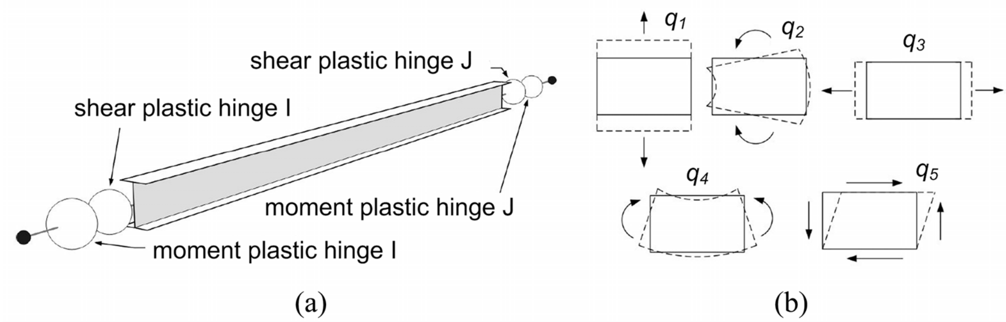

Figure 7. (a) The beam-column element and (b) the five deformation modes of panel element.

deformation modes (Figure 7b). Only the shear deformation can produce inelastic behavior (Lin et al., 2009). The panel elements used in this numerical model are elastic because the inelastic deformations are expected to occur only at the first floor. The column bases are fixed. All the beam-column connections are simulated as moment connections. The slabs are simulated as rigid diaphragms and the story mass is lumped at the geometric center of each floor plan. P-Δ effect is considered in the numerical model. Rayleigh damping, with the first two x-directional vibration modes with specified damping ratios, is used to simulate the inherent damping of the building. The specified damping ratios were calibrated according to the shaking table test results.

Considering that the columns affect the overall seismic response more significantly than beams, the degrading material, a more sophisticated inelastic material model, is used for the columns, and the bilinear material, a simpler inelastic material model, is used for the beams. The degrading material is capable of simulating strength and stiffness degradations and pinch phenomenon, whereas the bilinear material lacks these capabilities. Figure 8a shows the numerical model, labeled with the element types and material models. Figure 8b shows the bilinear material model used for the beams. The bilinear material model is a function of the initial Young's modulus, E; the yielding stress, F_y; and the post-yielding stiffness ratio, α (Figure 8b). The degrading material model uses three additional parameters, denoted as S_1, S_2, and S_3 (Figure 8c), to define the hysteretic rules for stiffness degradation, strength degradation, and pinching, respectively (Lin et al., 2009). Rather than represent the stress–strain relationships of concretes or steels, which are necessary for fiber beam-column elements, the material models (Figure 8b and c) are combined with the section properties to define the overall force-deformation relationship of a cross section of a beam-column element. Accordingly, the flexibility matrices of the plastic hinges at the two ends of the beam-column element are step-by-step updated in the computation process of Newmark-β numerical integration (Tsai and Lin, 2003). The backbone curve (Figure 8d) proposed by Ibarra et al. (2005) and FEMA P695 (Federal Emergency Management Agency (FEMA), 2009) was employed to determine the values of E, F_y, and α used in both of the bilinear and degrading material models. In addition, the values of the three parameters S_1, S_2, and S_3 used in the degrading material model were obtained from the component test results (Figure 4f and g). The computation of the parameters E, F_y, α, S_1, S_2, and S_3 is described below.

It is clear that the backbone curve (Figure 8d) is established in terms of three points: the yielding point (θ_y, M_y), the capping (peak) point (θ_{cap}, M_c), and the point with zero

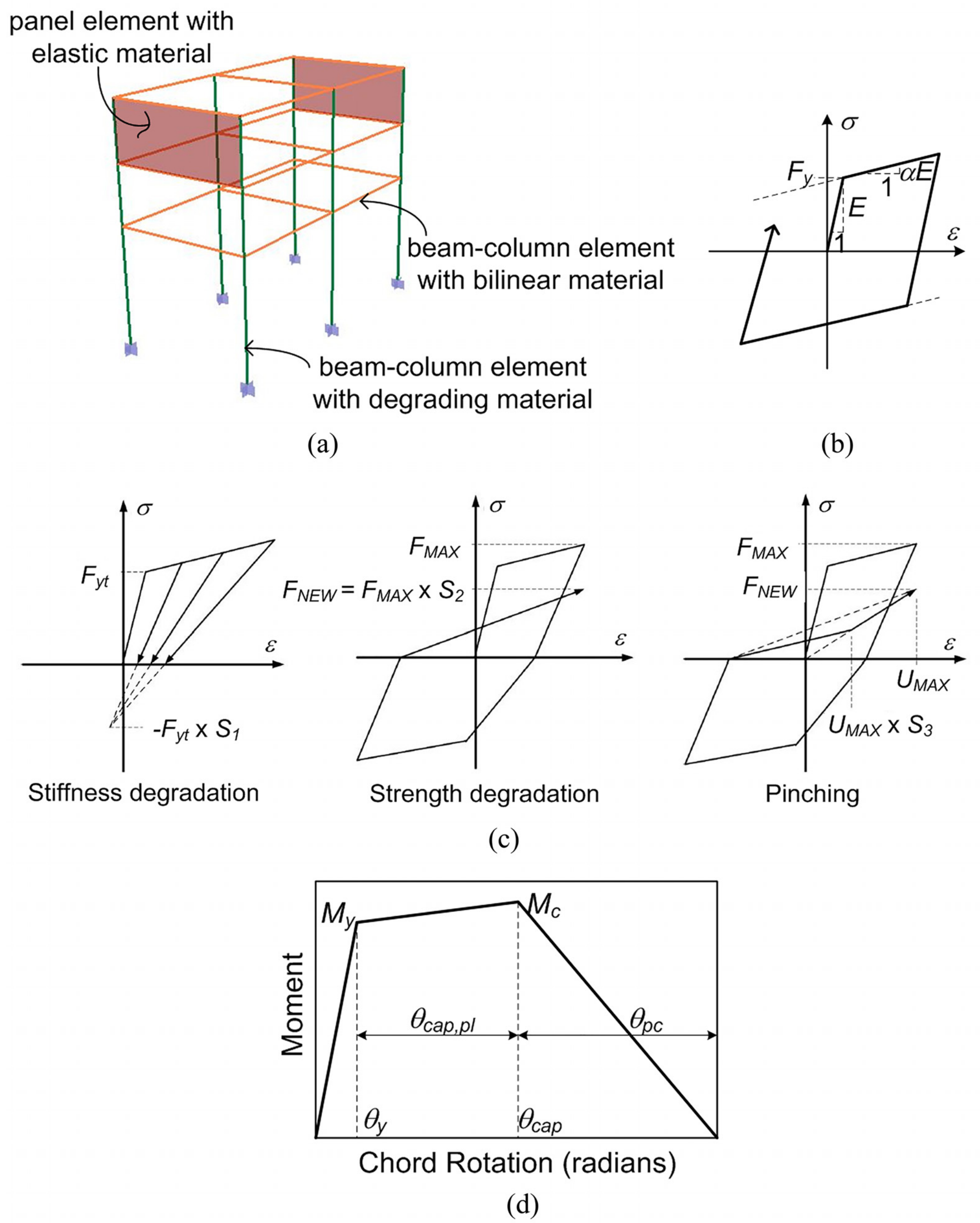

Figure 8. (a) The numerical model, (b) the stress (σ)—strain (ε) relationship of the bilinear material model, (c) parameters S_1, S_2, and S_3 for defining the hysteretic rule of the degrading material, and (d) a sketch of the backbone curve used for the RC beam-column elements.

strength (θ_{cap} + θ_{pc}, 0). The formulas for computing θ_y and M_y are available in Panagiotakos and Fardis (2001). Moreover, the formulas for computing θ_{cap}, θ_{pc}, and M_c are available in FEMA P695 (FEMA, 2009). It is worth noting that the formulas for computing the backbone curve are functions of the member's axial load. That is to say, the

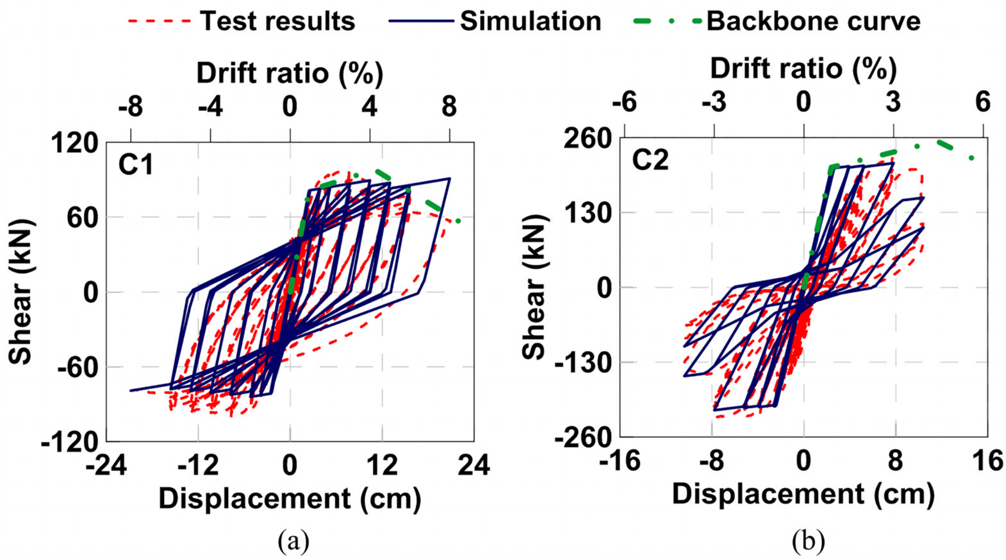

Figure 9. The simulated hysteretic loops of columns (a) C1 and (b) C2, compared with the single-column cyclic test results and the backbone curves.

effect of the varied axial load from story to story is reflected in the backbone curves. Based on the slope of the elastic segment of the backbone curve, that is, M_y/θ_y, and the slope-deflection method for double-curvature deformation, the effective section rigidity, $(EI)_{eff}$, of the RC beam-column elements is computed as $(M_y l)/(6\theta_y)$, where l is the element's length. As the section properties of a beam–column element, including the moment of inertia (denoted as I) and the section modulus (denoted as S), are given, the values of the initial Young's modulus E and yielding stress F_y are computed as $(EI)_{eff}/I$ and M_y/S, respectively. The post-yielding stiffness ratio α is equal to the ratio between the slopes of the second and the first segments of the backbone curve, that is, $(M_c–M_y)/(\theta_{cap}–\theta_y)/(M_y/\theta_y)$. For calibrating the values of the parameters S_1, S_2, and S_3, a single beam-column element model, subjected to the cyclic displacement history shown in Figure 4e, was analyzed using PISA3D. The details of the element, for example, the size, the boundary conditions, and the applied axial load, were identical to those of the component test. The values of S_1, S_2, and S_3 were determined by trial and error until the analytical hysteresis loops were satisfactorily consistent with those obtained from the component tests (Figure 4f and g). Figure 9a and b show the simulated hysteretic loops of the columns C1 and C2, respectively, compared with the component test results. Figure 9 indicates that the degrading material used in the PISA3D program satisfactorily simulates the cyclic behaviors of columns C1 and C2. The simulated hysteresis loops (Figure 9) were considered the best obtainable from trial and error, even though the hysteresis loop of column C1 in the positive direction is not very similar to the single-column cyclic test result. Figure 9 shows that column C2 degrades at a lesser inter-story drift, compared with column C1. Therefore, the replication of the hysteresis loop of column C2 is more critical than that of column C1 when simulating the failure of the three-story building.

Table 3 shows the values of the three nodes of the backbone curves for the columns and beams of the three-story building model. The values listed in Table 3 were computed

Table 3. The values of the three nodes of the backbone curves established for the columns and beams of the three-story building model

Element	Location	θ_y (rad.)	θ_{cap} (rad.)	θ_{pc} (rad.)	M_y (kN-m)	M_c (kN-m)	$P/(A_g f_c')$	$(EI)_{eff}/E_c I_g$
Column C1	1F_ext.[a]	0.0099	0.0484	0.1	87.97	107.33	0.033	0.287
	1F_int.[a]	0.0101	0.0464	0.1	94.50	114.87	0.065	0.302
	2F_ext.	0.0061	0.0455	0.1	85.50	104.47	0.021	0.224
	2F_int.	0.0062	0.0442	0.1	89.61	109.23	0.041	0.232
	3F_ext.	0.0061	0.0463	0.1	83.22	101.82	0.010	0.219
	3F_int.	0.0061	0.0456	0.1	85.29	104.23	0.020	0.223
Column C2	1F_ext.	0.0099	0.0486	0.1	247.29	302.44	0.013	0.320
	1F_int.	0.0100	0.0478	0.1	253.88	310.03	0.026	0.326
	2F_ext.	0.0062	0.0452	0.1	244.75	299.50	0.008	0.253
	2F_int.	0.0062	0.0446	0.1	249.32	304.78	0.017	0.257
	3F_ext.	0.0062	0.0455	0.1	242.71	297.15	0.004	0.252
	3F_int.	0.0062	0.0452	0.1	244.75	299.50	0.008	0.253
Beam	Beam	0.0093	0.0397	0.1	216.33	264.98	0	0.441

[a]ext. and int. denote the exterior and the interior columns, respectively.

according to the formulas provided in Panagiotakos and Fardis (2001) and FEMA (2009). $\theta_{cap,pl}$ as illustrated in Figure 8d is equal to θ_{cap}–θ_y. For brevity, $\theta_{cap,pl}$ is not shown in Table 3. In addition, because the details (i.e. the sizes, the reinforcements, and zero axial load) of all beams are identical, only one backbone curve is needed for all beams (Table 3). Moreover, because the walls are simulated using elastic panel elements, it is not necessary to construct the backbone curves of the walls. It is worth noting that the average values of $(EI)_{eff}/E_c I_g$ for columns and beams used in the three-story building model are 0.263 and 0.441, respectively, where E_c is the concrete's Young's modulus and I_g is the gross section moment of inertia. These results are in line with the statistics (Panagiotakos and Fardis, 2001) that the average effective rigidity of cracked RC members to yielding is approximately 20% of that of the uncracked gross section. Table 3 also clearly indicates that the connections of columns C1 with beams are weak-column-to-strong-beam, whereas the connections of columns C2 with beams are strong-column-to-weak-beam. The weak-column-to-strong-beam connection, which is clearly against the provisions of the seismic design code (American Society of Civil Engineers (ASCE), 2010; CPAMI, 2011), is intended to be identical to that of the collapsed buildings in the Meinong earthquake. Hence, it is rational to expect that at the column C1-to-beam connections, the possible plastic hinges will form at columns. On the contrary, at the column C2-to-beam connections, the possible plastic hinges will form at the ends of beams. The cyclic pushover of the numerical model with the backbone curves (Table 3) and the calibrated degrading material (Figure 9) was also conducted. Cyclic displacements, the same as those applied to the single-column cyclic tests (Figure 4e), were used as the control displacements at the roof's center of mass. The triangular load distribution, which is used for the code-specified static analysis (ASCE, 2010; CPAMI, 2011), was adopted in this inelastic static analysis. The ratio of the lateral loads ($w_i h_i / \sum_{x=1}^{3} w_x h_x$, $i = 1$ to 3) between the third, second, and first stories are 0.411: 0.342: 0.248, where w_i is the weight of the ith story, and h_i is the height of the ith story measured from the ground. Figure 10 shows the attained cyclic pushover curve, that is, the relationship between the base shear and roof displacement. Figure 10 indicates that the peak base shear is 687 kN.

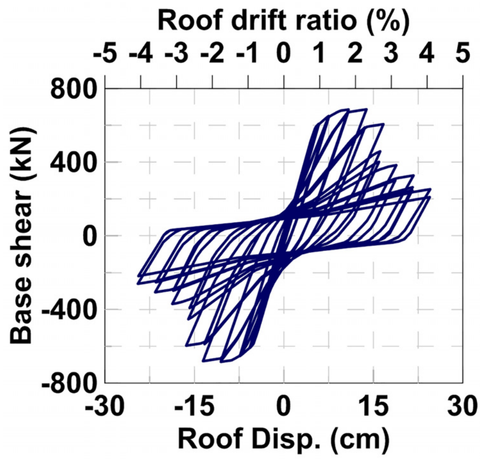

Figure 10. The cyclic pushover curve of the three-story building.

Table 4. The modal properties of the three-story building

Mode n		1	2	3	4	5	6	7	8	9
T_n (s)		0.395	0.321	0.196	0.071	0.068	0.045	0.024	0.017	0.011
Participation mass ratio (%)	x-trans.	98.63	0	0	1.38	0	0	0	0.0004	0
	y-trans.	0	63.56	29.94	0	5.38	0.46	0.59	0	0.0047
Participation mass moment of inertia ratio (%)	z-rot.	0	33.07	65.34	0	0.04	1.56	0.14	0	0.0001

The eigenvalue analysis results (Table 4) indicate that the first three x-directional vibration modes are the first, fourth, and eighth vibration modes, whose vibration periods are 0.395, 0.071, and 0.017 s, respectively. Figure 5f indicates that the first vibration period of the building coincides with one of the two periods, corresponding to obvious peaks of the x-directional pseudo-acceleration spectrum of TCU052. In addition, the first mode overwhelmingly dominates the x-directional vibrations because its participation mass ratio is up to 98.63% (Table 4). Note that other than these x-directional vibration modes, the vibration modes are y-directional translation-rotation coupled because the building is plan-asymmetric in the y-direction. The mode shapes of the first six vibration modes are shown in Figure 11, in which the rotational components are multiplied by the width of the building along the x-direction, that is, 350 cm and denoted as a. The first mode shape (Figure 11a) indicates that most of the x-directional deformation concentrates at the first story due to the added RC walls at the third story. In addition, the deformations at the second and third stories are relatively small and almost zero, respectively (Figure 11a). This indicates that the first story is a relatively soft story, where the deformation demand is much greater than other stories. In addition, the RC walls at the third story provide significant torsional stiffness, whereas the RC walls almost have no contribution to the y-translational stiffness. Therefore, it is noted that the rotational deformations at the third story are negligible, whereas there are certain amounts of y-directional deformations at the third story (Figure 11b, c, e, and f).

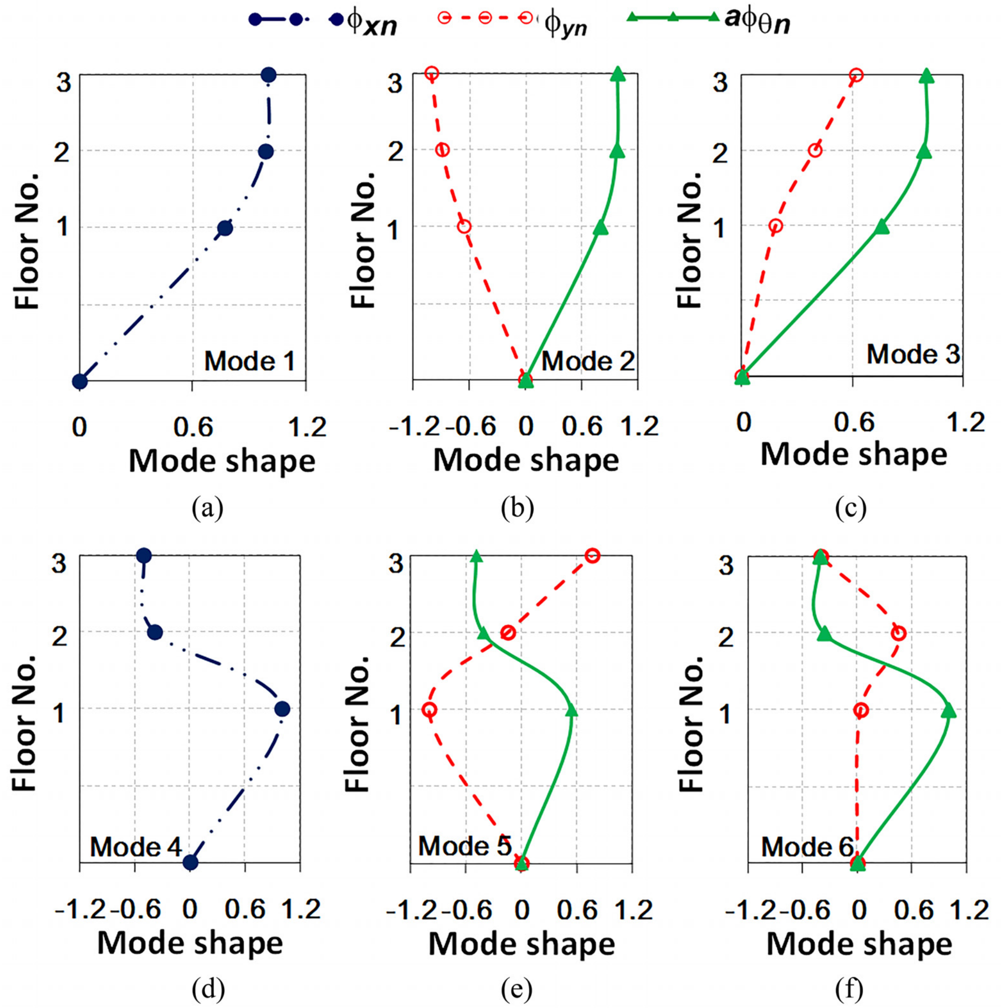

Figure 11. The mode shapes of the (a) 1st, (b) 2nd, (c) 3rd, (d) 4th, (e) 5th, and (f) 6th vibration modes of the three-story building.

Simulation results

For brevity, only one of the two shakings in each test level is shown herein. They are CHY047 (PGA = 420 gal) and TCU052 (PGA = 1000 gal) for the elastic and inelastic test levels, respectively. In addition, except for special cases, the corresponding PGAs shown in the parentheses are not written when the two shakings are mentioned hereafter. In order to take the possible structural damages caused by TCU052 (PGA = 800 gal) into account, the two shakings in the inelastic level were successively analyzed. That is to say, the measured acceleration record of TCU052 (PGA = 1000 gal) is appended at the end of that of TCU052 (PGA = 800 gal) as the integrated input ground motion record used in the PISA3D analysis. Figure 12a and b show the roof's displacement and acceleration, respectively, when the building was shaken by CHY047, compared with the simulation results. Likewise, Figure 12c and d are those for the building shaken by TCU052. Note

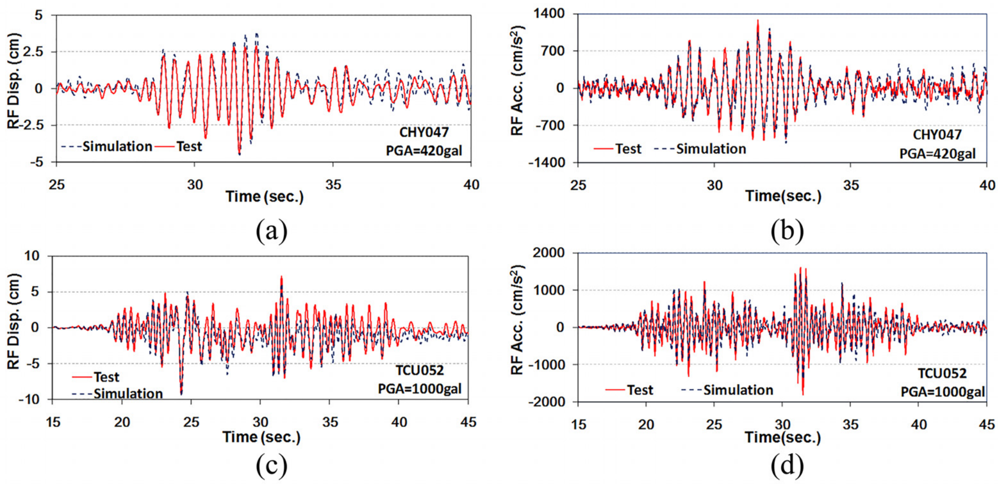

Figure 12. The (a) roof displacement and (b) roof acceleration of the building shaken by CHY047. The (c) roof displacement and (d) roof acceleration of the building shaken by TCU052.

that even though the numerical model subjected to TCU052 (PGA = 800 gal) and TCU052 (PGA = 1000 gal) was successively analyzed, only the seismic responses corresponding to TCU052 (PGA = 1000 gal) are illustrated. Figure 12 indicates that the simulation results are satisfactorily similar, both in phase and in the peak responses, to the physical test results. The closely matched phases imply that the fundamental vibration period computed from the numerical model, 0.395 s (see Table 4), is relatively accurate. By calibrating the simulation results, the damping ratios of the first two x-directional modes (i.e. vibration modes 1 and 4) used in the elastic (CHY047) simulations are 1.5%, and those used in the inelastic (TCU052) simulations are 3%. The greater inherent damping ratio used in the more severe shaking (i.e. TCU052) appears reasonable because the frictions between interfaces, such as the micro cracks beyond the plastic hinge regions and the contact surfaces between pedestals and the shaking table, increased. Figure 13 show the inter-story drifts of the three stories of the building shaken by CHY047 and TCU052. Comparing the inter-story drifts obtained from the tests and simulations (Figure 13) indicates that the numerical model is rather competent in simulating the elastic as well as the inelastic seismic responses. In addition, the large peak inter-story drift, 0.0249 rad, shown in Figure 13f implies that the building went into significant inelastic excursions under shaking TCU052. The relationships between the roof displacement and base shear of the numerical model shown in Figure 14a and d infer that the building was elastic and damaged under shakings CHY047 and TCU052, respectively. Figure 14b, c, e and f show the hysteretic loops of the first-story interior columns C1/C2 of the numerical model under shakings CHY047 and TCU052, respectively. The peak chord rotation shown in Figure 14e and f, which is equal to the first-story drift, is 0.0271 rad. Hence, the first story displacement is 8.13 cm ($= 0.0271 \times 300$), which takes 84.7% of the peak roof displacement of 9.6 cm (Figure 14d). This means that most of the lateral deformation concentrates on the first story. Figure 15 shows the snapshot of the deformation shape and the corresponding distribution of plastic rotations as the numerical model reached the peak roof displacement under shaking TCU052. The scale factor used for plotting the deformation (Figure 15) is equal to one. The size of the red reference circle at the bottom of Figure 15 indicates

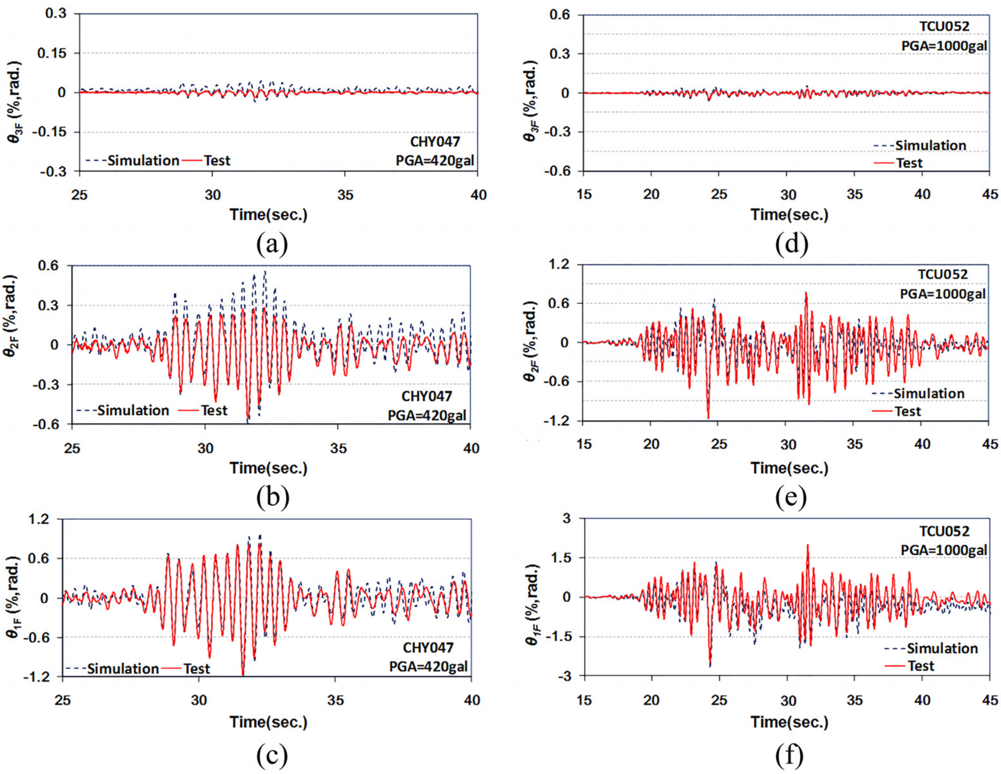

Figure 13. The inter-story drifts of the (a) third, (b) second, and (3) first stories of the building shaken by CHY047. The inter-story drifts of the (d) third, (e) second, and (f) first stories of the building shaken by TCU052.

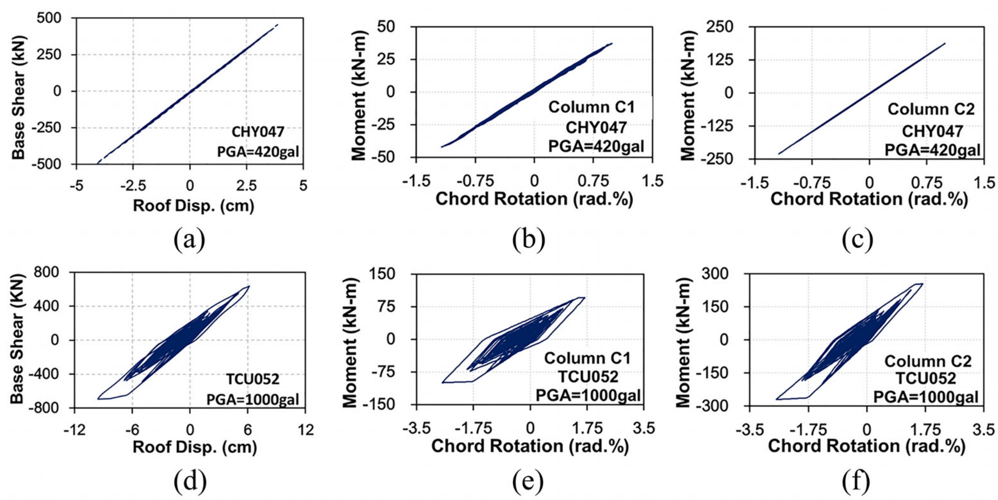

Figure 14. (a) The relationship between base shear and roof displacement, (b) the hysteresis loops of the first-story interior columns C1 and (c) C2 of the numerical model under shaking CHY047. (d), (e), and (f) are the counterparts of (a), (b), and (c), respectively, with the numerical model under shaking TCU052.

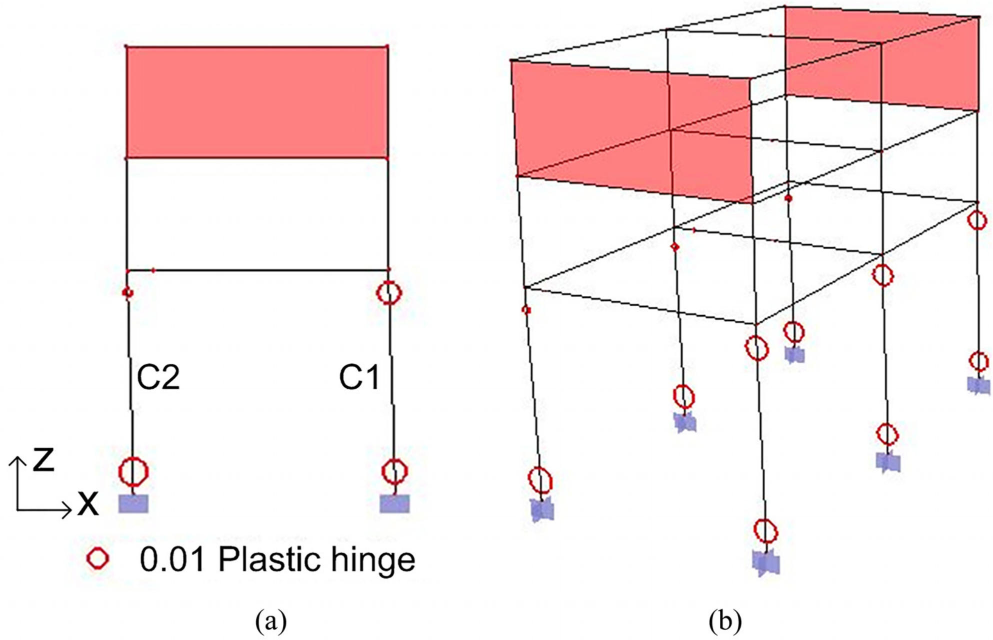

Figure 15. (a) The side view and (b) the perspective view of the snapshot of the deformation shape and the corresponding distribution of plastic rotations as the numerical model reached the peak roof displacement under shaking TCU052.

a 0.01 plastic rotation. The values of the plastic rotations at the bottom/top of columns C1 and C2 are 0.0122/0.0116 rad and 0.0145/0.0004 rad, respectively. The relative sizes of the red circles shown in the numerical model (Figure 15) reflect the aforementioned amounts of plastic rotation. Figure 15 also shows that all of the beams are elastic or essentially elastic. This is similar to the experimental results, which showed only slight damage to the beams (Figure 6c). It is clear that the likely collapse mechanism of this vertically irregular building would be formed at the first story. According to Table 3 and Figure 9, the capacities of plastic rotations at the peak (capping) points, that is, θ_{cap}–θ_y, for all columns are between 0.03 and 0.04 rad. This indicates that TCU052 needs to be further amplified until this building is shaken to collapse.

Table 5 shows the peak values of the roof acceleration, roof displacement, and the inter-story drift of the first story of the building, denoted as $\ddot{u}_{r,max}$, $u_{r,\ max}$, and θ_{max}, respectively, when subjected to CHY047 and TCU052 in comparison with those obtained from the simulation. It is worth noting that in the case of the three-story building, the peak inter-story drift of the first story is the peak inter-story drift among the three stories. The positive and negative errors in Table 5 show that the corresponding simulation results are overestimated and underestimated, respectively, compared with the tests results. Table 5 shows that most of the errors are within a ± 13% range. Consequently, Figures 12 and 13 and Table 5 validate the effectiveness of the numerical model in simulating the vertically irregular building. It is worth reporting that the analysis time spent using PISA3D for analyzing the building subjected to CHY047 and TCU052 (for single shaking with PGA = 1000 gal rather than successive shakings with PGA = 800 gal and 1000 gal) are 61.5 and 50.5 s.,

Table 5. The comparison of the peak responses obtained from the shaking table tests and the simulation results for (a) CHY047 and (b) TCU052

	$\ddot{u}_{r,max}$ (mm/s^2)	$u_{r,\ max}$ (mm)	θ_{max} (%, rad.)
(a) CHY047			
Test result	12,871	43.81	1.18
Simulation	11,250	45.53	1.18
Error (%)	−12.6	3.9	0.5
(b) TCU052			
Test result	18,219	92.75	2.49
Simulation	14,408	95.85	2.71
Error (%)	−20.9	3.3	9.0

respectively. The two runs of PISA3D were executed on a desktop computer with an Intel Core i7 central processing unit. This shows that PISA3D is very efficient in performing nonlinear response history analyses.

Seismic analysis of the vertically irregular building

The validated numerical model is further used as an example building to study two interesting issues of earthquake engineering. The two issues are associated with the effective section rigidities of RC beams/columns, and the effects of near-fault ground motions. This case study appears valuable because the example building is vertically irregular and its elastic/inelastic properties have been verified by using not only far-field but also near-fault ground motions generated from the shaking table.

Effective section rigidity

It is worth noting that different building codes or research suggest different effective section rigidities, $(EI)_{eff}$, of RC members. For example, ACI 318-08 (ACI Committee 318, 2008) specifies $0.35E_cI_g$ for beams and walls and $0.7E_cI_g$ for columns, whereas the FEMA 356 seismic rehabilitation guidelines (ASCE, 2000) specifies $0.5E_cI_g$ as $P/(A_gf_c') < 0.3$, and $0.7E_cI_g$ as $P/(A_gf_c') > 0.5$. A_g is the gross section area and P is the axial load. Moreover, Elwood and Eberhard (2006) suggested $0.2E_cI_g$ as $P/(A_gf_c') < 0.2$, and $0.7E_cI_g$ as $P/(A_gf_c') > 0.5$, with a linear transition between these two extremes. These aforementioned recommendations, which were supported by statistic results, are convenient for general use. In contrast, the numerical model, which elaborately sets specific backbone curves for each element, does not seem to be a common practice. Therefore, it is interesting to look into what the numerical model would yield if it is constructed as is done in common practice. The simple numerical model is a variation of the validated numerical model in which the columns and beams' $(EI)_{eff}$ are set as $0.2E_cI_g$. This is because of the small values of $P/(A_gf_c')$ for all columns (Table 3). This variation, that is, the reduction of $(EI)_{eff}$, elongated the fundamental vibration period from 0.395 s (see Table 4) to 0.51 s. The damping ratios of the simple numerical model are the same as those used in the original numerical model. In comparison with the test results, Figure 16a to c respectively show the roof acceleration, roof displacement, and the inter-story drift of the first story of the simple numerical model subjected to CHY047. Figure 16d to f are the counterparts of Figure 16a to c with the model being subjected to TCU052. Figure 16 as a whole indicates that the simple numerical model is not capable of simulating the 3-story building well in comparison with those

Table 6. The errors of the peak responses obtained using the validated numerical model and using the simple numerical model

Shaking	Numerical model	Error (%)		
		$\ddot{u}_{r,\ max}$	$u_{r,\ max}$	θ_{max}
CHY047	Validated	−12.6	3.9	0.5
	Simple	−5.4	75.3	66.9
TCU052	Validated	−20.9	3.3	9.0
	Simple	−41.4	22.2	23.3

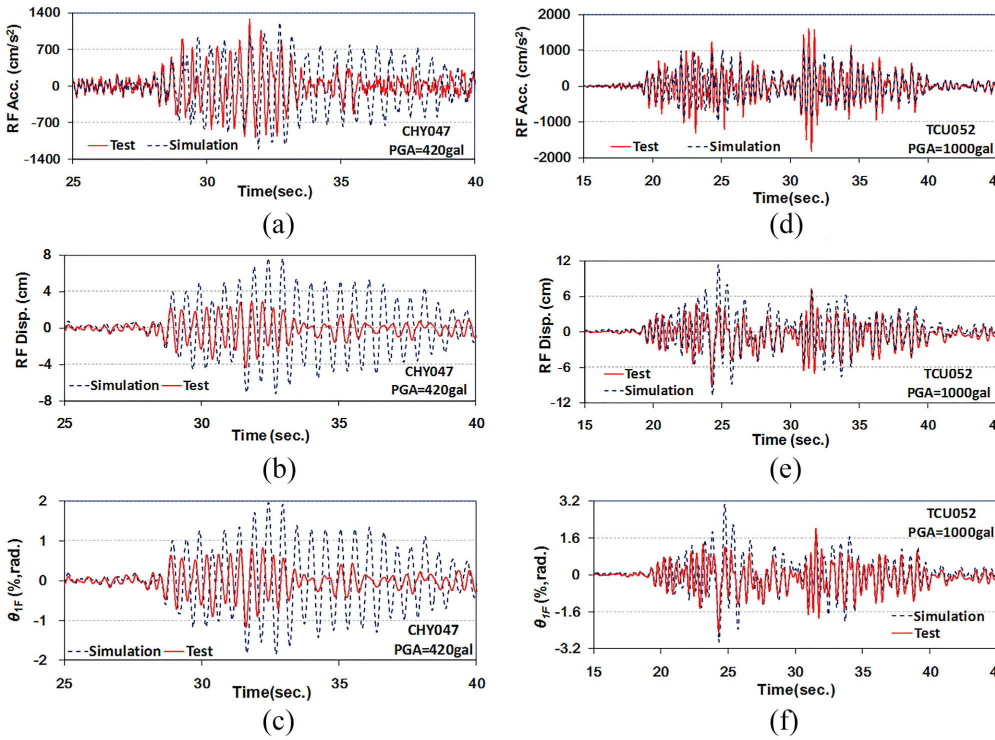

Figure 16. In comparison with the test results, (a) the roof acceleration, (b) the roof displacement, and (c) the inter-story drift of the first story of the simple numerical model subjected to CHY047. (d) The roof acceleration, (e) the roof displacement, and (f) the inter-story drift of the first story of the simple numerical model subjected to TCU052.

shown in Figures 12 and 13. The elongated fundamental vibration period of the simple numerical model causes the estimated responses of the building subjected to CHY047 to be significantly out of phase in comparison with the test results (Figure 16a to c). Nevertheless, Figure 16d to f show that the estimated responses of the building subjected to TCU052, except those during the 20th second to the 25th second, are only slightly out of phase in comparison with the test results. This implies that the inelastic properties of the simple numerical model dominate the estimated seismic responses of the building subjected to TCU052. Table 6 lists the errors of the peak responses obtained from the simple numerical model, compared with those obtained from the validated numerical model. It is worth noting that due to the elongation of the vibration period of the first mode, the roof displacements (Figure 16b and e) and the inter-story drifts of the first story (Figure 16c and f) are further overestimated using the simple numerical model (Table 6). This highlights that $(EI)_{eff}$ plays a critical role in the numerical models for RC buildings. It also implies that the expected seismic responses of RC buildings analyzed based on daily practice are very likely far from what the seismic responses really are. This is only a single case study of the adequacy of the commonly used effective section rigidity. Extensive study is needed to provide concrete suggestions for improving this common practice.

Effects of the TCU052 near-fault ground motion

The primary task of the shaking table (Figure 1b), which has both high-velocity and long-stroke capacities (Table 1), is to simulate near-fault ground shakings. Although the 3-story building was not shaken to collapse on the grand-opening date of the NCREE Tainan lab, it is interesting to examine the extremes of the building subjected to the selected near-fault ground motion, TCU052, via analytical approaches. Therefore, the validated numerical model is further analyzed by using the incremental dynamic analysis (IDA) method (Vamvatisikos and Cornell, 2002, 2004). Although an analysis of the seismic responses of the building, when it is subjected to an ensemble of near-fault ground motion records rather than only TCU052, would be more representative, the IDA performed in this study was carried out on the numerical model subjected to only CHY047 and TCU052. This is because the analysis results of the numerical model subjected to CHY047 and TCU052 have been verified by the shaking table tests. Even if the numerical model is subjected to an ensemble of near-fault ground motion records, it is challenging to generalize the characteristics of the seismic responses of buildings with soft-and-weak first stories subjected to near-fault ground motions.

The measured TCU052 acceleration records on the shaking table's top surface (Figure 5c and d) are still used as the input ground motions. Therefore, not only the x-directional, but also the z-directional (vertical) excitations are simultaneously exerted on the numerical model. The peak inter-story drift, θ_{max}, is used as the engineering demand parameter, that is, the abscissa of the IDA curves. The 5% damped first-mode spectral acceleration, denoted as $S_a(T_1, 5\%)$, is used as the intensity measure (IM), that is, the ordinate of the IDA curves. It is worth noting that the damping ratio of the intensity measure (i.e. 5%) is not necessarily the same as the inherent damping ratio of the building because $S_a(T_1, 5\%)$ is merely a measure of the intensity of ground motions. While scaling the ground motion records, the same scaling factor is applied to both the x-directional and the z-directional components of the ground motion records. For the purpose of comparison, CHY047 (Figure 5a and b), a far-field ground motion record, is also adopted to construct the IDA curves. Both CHY047 and TCU052 are scaled from $S_a(T_1, 5\%) = 0.25$–5.0 g with an increment of 0.25 g. Therefore, there are 20 nonlinear response history analyses for the construction of each IDA curve. In addition, Rayleigh damping with 3% damping ratios of the first and the fourth vibration modes is used to represent the inherent damping of the building.

Figure 17a and b show the IDA curves of the validated numerical model subjected to CHY047 and TCU052, respectively. Both Figure 17a and b indicate that the first story's inter-story drift increases much more rapidly as the IM, that is, $S_a(T_1, 5\%)$, increases, in comparison with the second and third stories. This means that the deformation

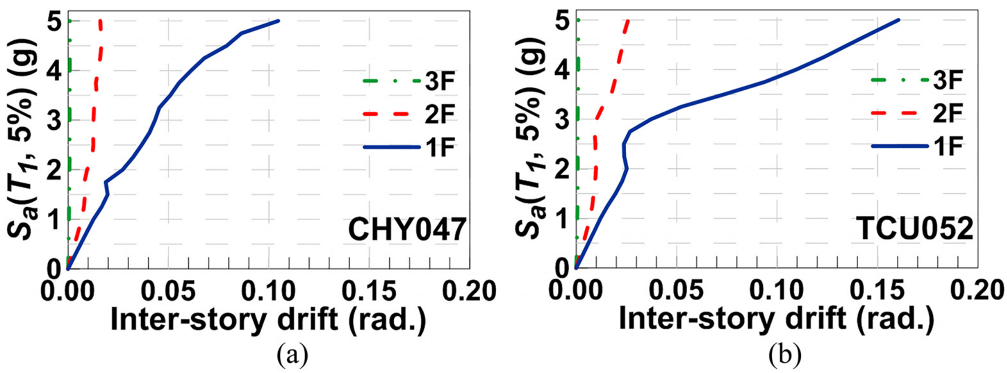

Figure 17. The IDA curves for (a) CHY047 and (b) TCU052.

concentrates on the soft-and-weak first story, and the collapse mechanism of this numerical model eventually forms at the first story. The slopes of the IDA curves (Figure 17a and b) indicate that the numerical model is elastic or essentially elastic as the value of $S_a(T_1, 5\%)$ is not larger than 1.25 g. In addition, there are obvious phenomena of "structural resurrection" (Vamvatisikos and Cornell, 2002) while $S_a(T_1, 5\%)$ increases from 1.5 to 1.75 g and from 2.0 to 2.5 g for CHY047 (Figure 17a) and TCU052 (Figure 17b), respectively. In other words, the inter-story drifts do not increase and even conversely decrease while the IM, that is, $S_a(T_1, 5\%)$, increases within the aforementioned ranges. Beyond the structural resurrection, the decrease of the IDA curve slope is gradual and moderate under the excitation of CHY047 (Figure 17a), whereas the decrease of the IDA curve slope is rapid and excessive under the excitation of TCU052 (Figure 17b). This implies that the three-story building is prone to be completely destroyed or collapsed by the near-fault ground motion TCU052 once the seismic intensity is beyond that which causes structural resurrection. In contrast, under the far-field ground motion CHY047, the three-story building still preserves substantial seismic resistance even though the seismic intensity is beyond that which causes structural resurrection. Taking the tangent slope of an IDA curve equal to 20% of its initial slope as the indicator of building collapse, Figure 17a and b infer that the three-story building is collapsed at $S_a(T_1, 5\%) = 4.75$ and 3.25 g under the excitations of CHY047 and TCU052, respectively.

Figure 18a and b show the distribution of the inter-story drifts along the building height under the excitations of CHY047 and TCU052, respectively. For clarity, only six curves, which correspond to $S_a(T_1, 5\%) = 0.5$, 1, 2, 3, 4, and 5 g, are shown in each plot of Figure 18a and b. Because the numerical model is elastic at $S_a(T_1, 5\%) = 0.5$ and 1 g, the increments of the inter-story drifts from $S_a(T_1, 5\%) = 0.5$ to 1 g are proportional between stories. Nevertheless, the increments of the inter-story drifts from $S_a(T_1, 5\%) = 2$ to 5 g are no longer proportional between stories because the numerical model becomes inelastic. The increment of the first story's inter-story drift is most significant when $S_a(T_1, 5\%)$ varies from 4 to 5 g (Figure 18a) and from 3 to 4 g (Figure 18b) under the excitations of CHY047 and TCU052, respectively. These two aforementioned ranges separately bracket the two values of $S_a(T_1, 5\%)$ equal to 4.75 and 3.25 g, which cause the building collapse under CHY047 and TCU052, respectively.

Figure 19a and b show the relationships between $S_a(T_1, 5\%)$ and the story shears of the numerical model subjected to CHY047 and TCU052, respectively. It is interesting to note

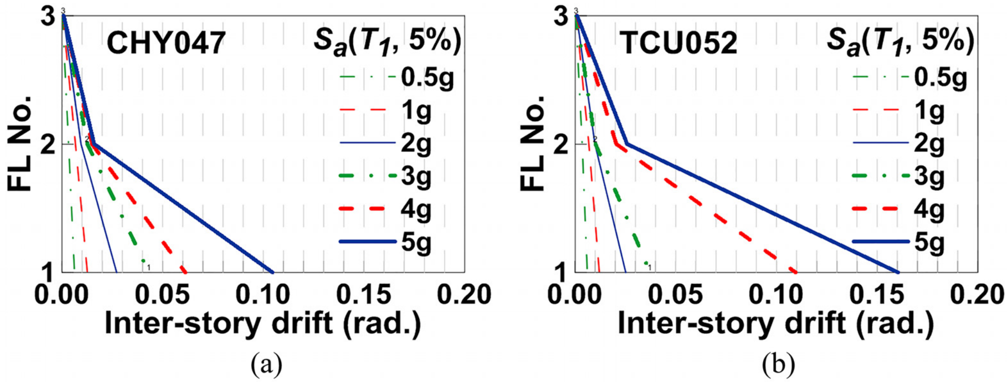

Figure 18. The distribution of the inter-story drifts along the building height under the excitations of (a) CHY047 and (b) TCU052.

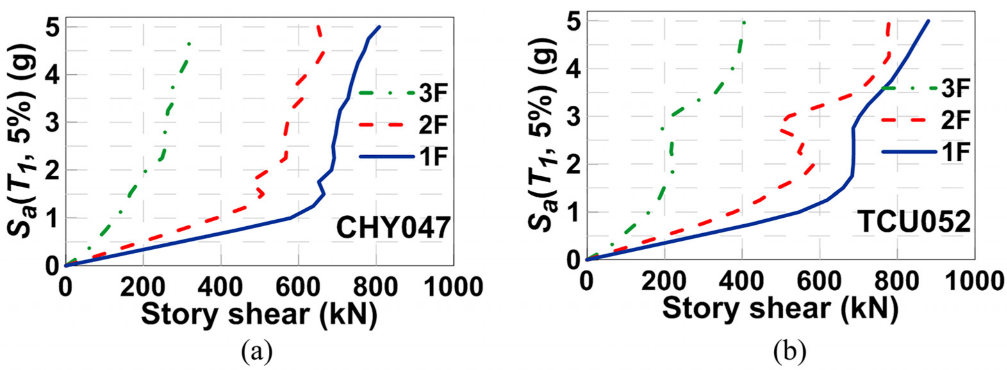

Figure 19. The relationships between $S_a(T_1, 5\%)$ and the story shears of the numerical model subjected to (a) CHY047 and (b) TCU052.

that the story shears of the first and the second stories decrease as $S_a(T_1, 5\%)$ of CHY047 varies from 1.5 to 1.75 g (Figure 19a), which is the same range of structural resurrection observed from Figure 17a. Similarly, Figure 19b shows that the story shear of the second story decreases as $S_a(T_1, 5\%)$ of TCU052 varies from 2 to 2.75 g, which approximates the range of structural resurrection observed from Figure 17b. In summary, the leftward dents shown in Figure 19a and b are related to the structural resurrection observed from the IDA curves (Figure 17a and b). The decrease of the story shears reasonably reflects the decrease of the inter-story drifts during the structural resurrection. It is clear that the difference between the story shears of the two successive stories is the lateral load applied on the lower story. Therefore, Figure 19a and b clearly indicate that the lateral load applied on the first story is obviously smaller than those applied on the second and the third stories. In addition, when $S_a(T_1, 5\%)$ of TCU052 is beyond 3.25 g, which is the seismic intensity causing the building collapse, the lateral load applied on the first story is significantly lessened in comparison with the lateral loads applied on the second and the third stories (Figure 19b).

Figure 20a shows the point in time, when the peak roof displacement occurs, corresponding to different $S_a(T_1, 5\%)$ of CHY047. Figure 20b to g show the six roof

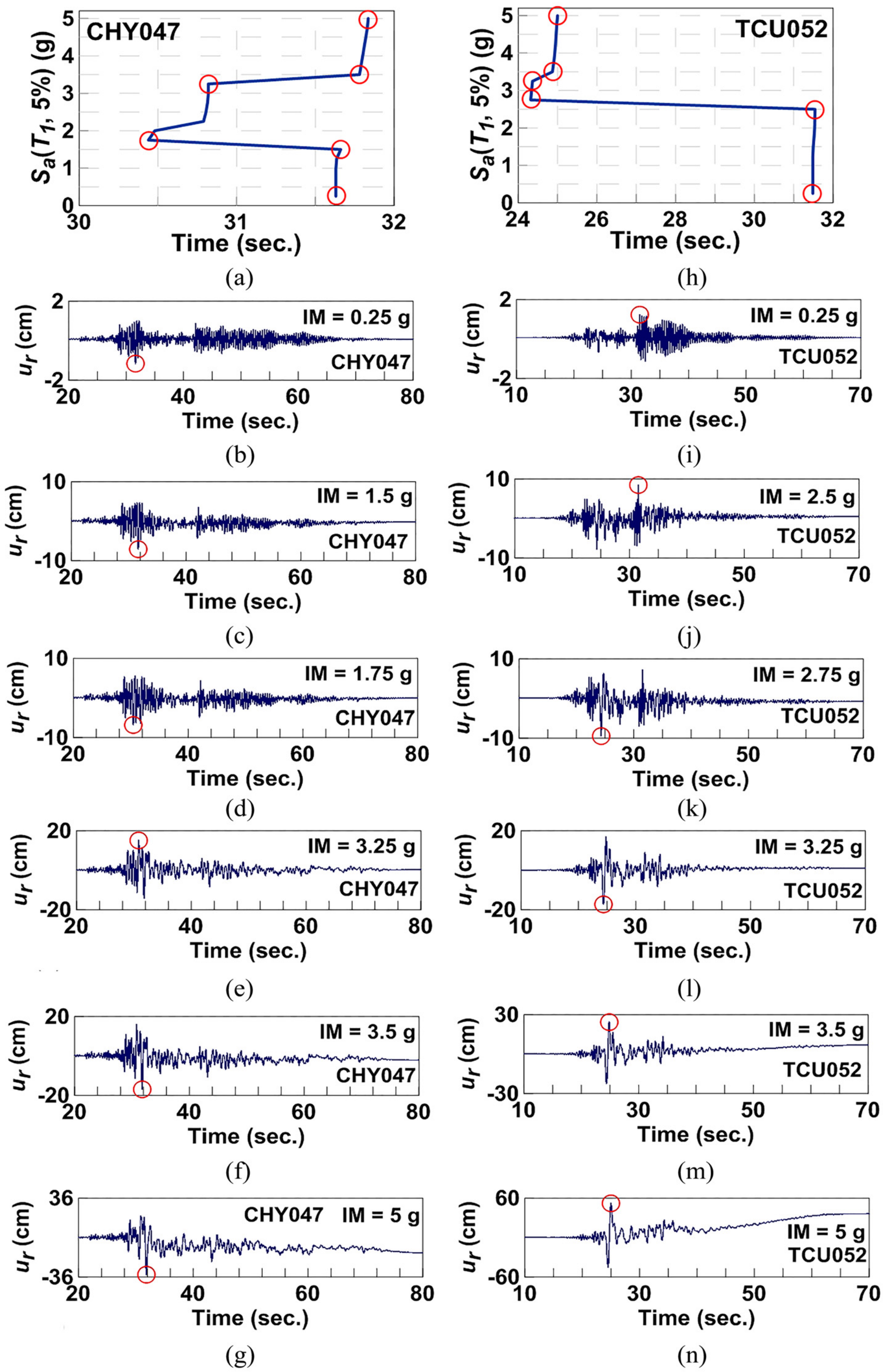

Figure 20. (a) The occurrence time of the peak roof displacement of the numerical model subjected to CHY047 with $S_a(T_1, 5\%)$ ranging from 0.25 to 5 g. (b) to (g) are the roof displacement histories corresponding to six intensity levels of CHY047. (h) The occurrence time of the peak roof displacement of the numerical model subjected to TCU052 with $S_a(T_1, 5\%)$ ranging from 0.25 to 5 g. (i) to (n) are the roof displacement histories corresponding to six intensity levels of TCU052.

displacement histories corresponding to the six red circles indicated in Figure 20a. The red circle in each plot of the roof displacement histories (Figure 20b to g) pinpoints the peak roof displacement. Figure 20a indicates that the time of interest is between the 30th second and the 32nd second. Note that the peak input ground acceleration of CHY047 occurs at 30.68 s (Figure 5a). Therefore, this means that no matter how the far-field ground motion CHY047 is scaled, the peak roof displacement always occurs around the time of the peak input ground acceleration. In addition, the most significant change of the time of interest happens as $S_a(T_1, 5\%)$ varies from 1.5 to 1.75 g (Figure 20a), within which structural resurrection also occurs (Figure 17a).

For the near-fault ground motion TCU052, the counterparts of Figure 20a to g are shown as Figure 20 h to n. Figure 20h indicates that the time of interest is between the 24th second and the 32nd second, which is a much wider range of time than that shown in Figure 20a. The most significant change of the time of interest happens as $S_a(T_1, 5\%)$ varies from 2.5 to 2.75 g (Figure 20h), which is subsequent to the $S_a(T_1, 5\%)$ that the structural resurrection occurs (Figure 17b). When $S_a(T_1, 5\%)$ is not less than 2.75 g, the time of interest is around 24.22 s, which is the time that the peak input ground acceleration of TCU052 occurs (Figure 5b). Nevertheless, when $S_a(T_1, 5\%)$ is not larger than 2.5 g, the time of interest is far later than 24.22 s (Figure 20h). Apparently, $S_a(T_1, 5\%)$ ranging from 2.5 to 2.75 g is a watershed of the time of interest for the numerical model subjected to the near-fault ground motion TCU052.

Figure 20l to n show that when the $S_a(T_1, 5\%)$ of TCU052 is not less than 3.25 g, there is a remarkable spike in each plot of the roof displacement histories. The spike is a two-side spike (i.e. possessing both positive and negative outstanding displacements). In addition, the magnitudes of the spike on both sides are almost equal. Note that the numerical model is collapsed at $S_a(T_1, 5\%) = 4.75$ and 3.25 g under the excitations of CHY047 and TCU052, respectively. Nevertheless, even when $S_a(T_1, 5\%)$ of CHY047 is scaled to 5 g, there is no such two-side spike in the plot of the roof displacement history (Figure 20g). Based on these observations in Figure 20g, l, m, and n, the two-side spike is a unique phenomenon for the numerical model subjected to TCU052 shaking.

For the purpose of simplifying the comparison between the effects of the two-side-spike and one-side-spike excursions, the one-side-spike excursion is idealized as a sine curve, $A \times sin(\omega_1 t)$, where t is from 0 to π/ω_1. Therefore, the displacement response is one-sided with a period of $2\pi/\omega_1$. The two-side-spike excursion is also idealized as a sine curve, $A \times sin(\omega_2 t)$, where t is from 0 to $2\pi/\omega_2$. Therefore, the displacement response is exactly two-sided with a period of $2\pi/\omega_2$. Two representative cases, $\omega_2 = \omega_1$, and $\omega_2 = 2\omega_1$, are considered. For $\omega_2 = \omega_1$, the two-side-spike excursion takes twice as long as the one-side-spike excursion (Figure 21a). For $\omega_2 = 2\omega_1$, the two-side-spike excursion takes the same amount of time as the one-side-spike excursion (Figure 21b). In both cases, the two-side-spike excursion results in a larger accumulative energy dissipation than the one-side-spike excursion. Therefore, according to the damage index proposed by Park and Ang (1985), the two-side-spike excursion causes more damage to structural components in comparison with the one-side-spike excursion. Furthermore, for the case of $\omega_2 = 2\omega_1$, the peak amplitude of the velocity resulting from the two-side-spike excursion is double that of the one-side-spike excursion. In addition, the peak amplitude of the acceleration resulting from the two-side-spike excursion is four times the peak amplitude resulting from the one-side-spike excursion. Therefore, in comparison with the one-side-spike excursion, the higher velocity and acceleration resulting from the two-side-spike excursion are likely to be more destructive to structures. Figure 22a and b show the energy histories, including strain

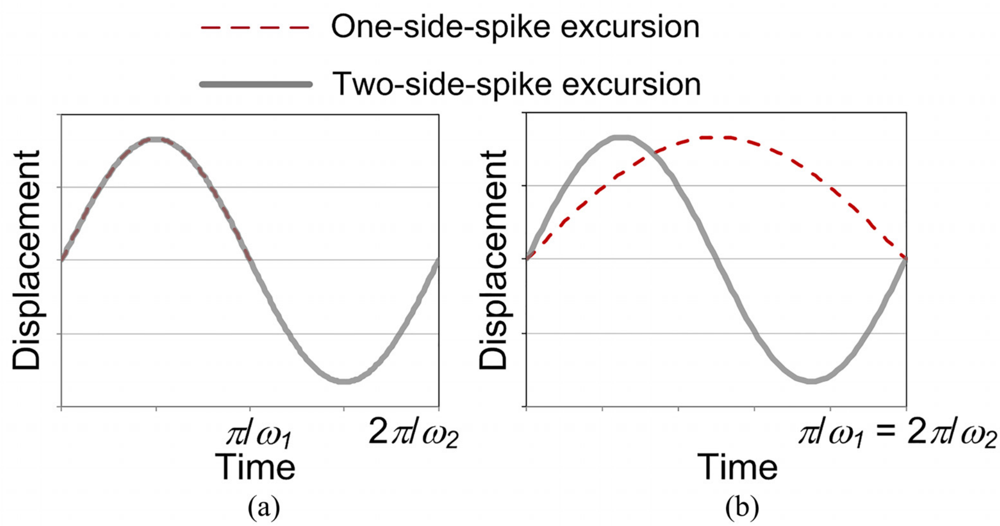

Figure 21. Two representative cases for comparing a two-side-spike excursion with a one-side-spike excursion: (a) $\omega_2 = \omega_1$, and (b) $\omega_2 = 2\omega_1$.

energy, denoted as E_s, damping energy, denoted as E_d, and kinetic energy, denoted as E_k, of the three-story building under CHY047 scaled to $S_a(T_1, 5\%) = 4.75$ g and TCU052 scaled to $S_a(T_1, 5\%) = 3.25$ g, respectively. Figure 22c and d are the zoomed-in plots of Figure 22a and b, respectively. In Figure 22, it is clear that the difference between $E_s + E_d + E_k$, that is, the input energy, and $E_s + E_d$ represents the kinetic energy E_k. In addition, the difference between $E_s + E_d$ and E_s represents the damping energy E_d. Comparing Figure 22b with Figure 22a shows that the kinetic energy history of the three-story building under TCU052 scaled to $S_a(T_1, 5\%) = 3.25$ g has a clear spike at approximately 25.5 second. As kinetic energy is related to structural velocity, this clear spike reflects the high velocity resulting from the two-sided spike observed from the roof displacement histories shown in Figure 20l. Figure 22 additionally shows that the input energy of the three-story building under TCU052 scaled to $S_a(T_1, 5\%) = 3.25$ g is less than and close to one half of that of the building under CHY047 scaled to $S_a(T_1, 5\%) = 4.75$ g. Nevertheless, both the base shears of the three-story building under CHY047 scaled to $S_a(T_1, 5\%) = 4.75$ g and TCU052 scaled to $S_a(T_1, 5\%) = 3.25$ g are close to 800 kN (Figure 19). Therefore, Figures 19 and 22 collectively imply that even though the input energy of the near-fault ground motion, that is, TCU052 scaled to $S_a(T_1, 5\%) = 3.25$ g, is only about one half of the input energy of the far-field ground motion, that is, CHY047 scaled to $S_a(T_1, 5\%) = 4.75$ g, the large acceleration (i.e. large force) resulting from the two-side-spike excursion is critical to the collapse of the three-story building. To the best of the authors' knowledge, the effect of the two-side spike has not been identified in existing literature. Further exploration may elucidate if the two-side spike is a common phenomenon in the displacement responses of buildings that are collapsed under near-fault ground motions.

Figure 23a illustrates the snapshot of the deformation and the corresponding distribution of plastic rotations as the numerical model reached the peak roof displacement under CHY047 scaled to $S_a(T_1, 5\%) = 4.75$ g. The scale factor used for plotting the

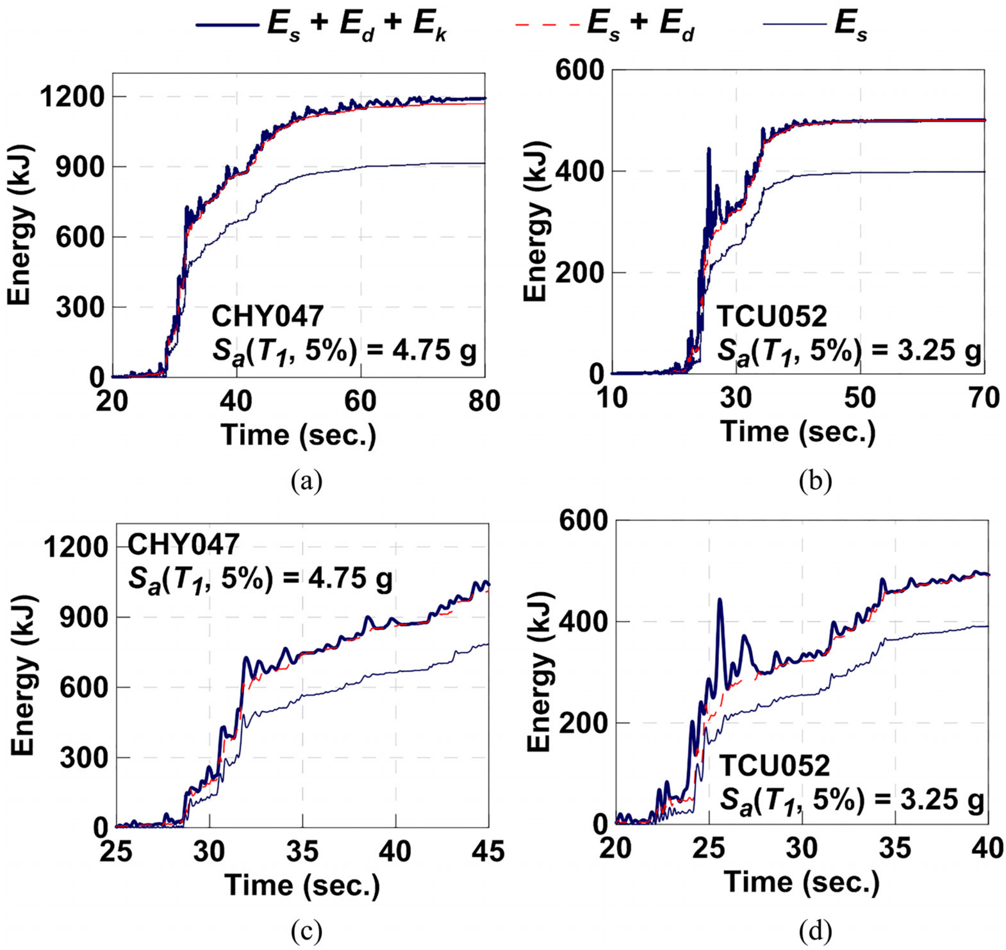

Figure 22. The energy histories of the three-story building under (a) CHY047 scaled to $S_a(T_1, 5\%) = 4.75$ g and (b) TCU052 scaled to $S_a(T_1, 5\%) = 3.25$ g. (c) and (d) are the zoomed-in plots of (a) and (b), respectively.

deformation (Figure 23a) is equal to one. Figure 23b and c are the positive and negative envelopes of the plastic rotations of the numerical model under the same shaking. Figure 23d to f are the counterparts of Figure 23a to c when the numerical model is excited by TCU052 scaled to $S_a(T_1, 5\%) = 3.25$ g. The plan frames shown in Figure 23 are the exterior frame, that is, the frames on column lines 1 and 3 (Figure 2a). Figure 23a to f show that beam/column members yield at seven locations under these two excitations. These seven locations are numbered from "1" to "7," as shown in Figure 23b. Table 7 lists the values of the plastic rotations, which are equal to the total rotation minus the yielding rotation, of these seven locations corresponding to each plot of Figure 23a to f.

Figure 23a to c indicate that the tops and bottoms of columns C1 and C2 of the first story are significantly yielded. The beam end connected to column C2 and the top and bottom of column C1 of the second story are also yielded, whereas the inelastic extents of these locations are much minor than those at the first story's columns. The plastic

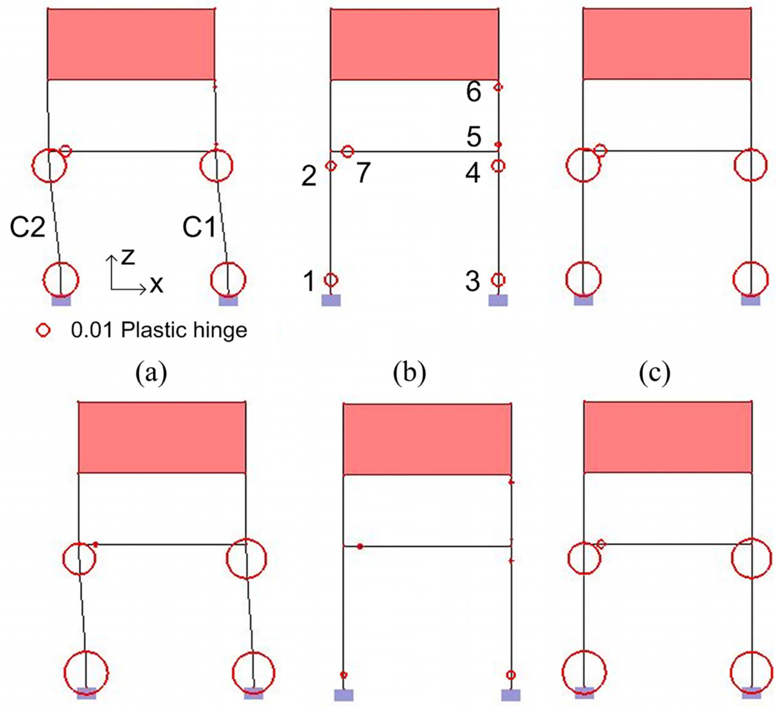

Figure 23. Under CHY047 scaled to $S_a(T_1, 5\%)$ = 4.75 g, (a) the snapshot of the deformation and the corresponding distribution of plastic rotations while the peak roof displacement occurs, and (b) the positive and (c) the negative envelopes of plastic rotations. (d), (e), and (f) are the counterparts of (a), (b), and (c) when the numerical model is excited by TCU052 scaled to $S_a(T_1, 5\%)$ = 3.25 g.

Table 7. The plastic rotations of the numerical model under the two shakings CHY047 (IM = 4.75 g) and TCU052 (IM = 3.25 g). The unit of the plastic rotations is radians (%)

Shaking	State	Location						
		1	2	3	4	5	6	7
CHY047 (IM = 4.75 g)	Peak roof disp.	–2.86	–2.76	–2.84	–2.65	0.25	0.14	0.90
	Positive envelope, $\theta^+_{pl,max}$	1.02	0.75	1.04	1.00	0.39	0.56	0.91
	Negative envelope, $\theta^-_{pl,max}$	–2.86	–2.76	–2.85	–2.65	0	0	–1.02
	$\frac{\max\left(\theta^+_{pl,max}, \left|\theta^-_{pl,max}\right|\right)}{\theta_{cap}-\theta_y}$	0.74	0.71	0.74	0.69	0.10	0.14	0.34
TCU052 (IM = 3.25 g)	Peak roof disp.	–3.59	–2.63	–3.44	–3.28	0	–0.04	0.37
	Positive envelope, $\theta^+_{pl,max}$	0.48	0	0.67	0.28	0.09	0.32	0.37
	Negative envelope, $\theta^-_{pl,max}$	–3.59	–2.63	–3.44	–3.28	0	–0.04	–0.66
	$\frac{\max\left(\theta^+_{pl,max}, \left|\theta^-_{pl,max}\right|\right)}{\theta_{cap}-\theta_y}$	0.93	0.68	0.89	0.85	0.02	0.08	0.22

IM: intensity measure.

rotations of the first story's columns illustrated in Figure 23a are between 2.65% and 2.86% radians (Table 7). Comparing the peak values of the plastic rotations with the values of $\theta_{cap} - \theta_y$ (Table 3), denoted as $\max\left(\theta^{+}_{pl,max}, \quad \left|\theta^{-}_{pl,max}\right|\right)/(\theta_{cap} - \theta_y)$ in Table 7, indicates that the first story's column rotations are similar to yet still less than θ_{cap} when the numerical model is subject to CHY047 scaled to $S_a(T_1, 5\%) = 4.75$ g.

Under near-fault ground motion TCU052 scaled to $S_a(T_1, 5\%) = 3.25$ g, the distributions of the plastic rotations of the numerical model (Figure 23d to f) are similar to those under CHY047 scaled to $S_a(T_1, 5\%) = 4.75$ g (Figure 23a to c). Nevertheless, the inelastic extents of the beam and the second story's column are less than the far-field shaking case (i.e. Figure 23a to c). Table 7 shows that the plastic rotations of the first story columns are larger than those in the far-field shaking case and almost equal to the values of $\theta_{cap} - \theta_y$ (Table 3). This confirms that the deformation and the corresponding plastic rotations illustrated in Figure 23d is a collapse mechanism. In other words, $S_a(T_1, 5\%) = 3.25$ g of TCU052 is indeed an incipient intensity causing the collapse of the numerical model. As a result, using the tangent slope of an IDA curve equal to 20% of its initial slope as the indicator of building collapse appears very appropriate for this near-fault ground shaking case.

Summary and conclusion

The NCREE Tainan lab is one of the few laboratories in the world that has the capacity to perform shaking table tests reflecting near-fault ground motions. On the opening date of the lab, a vertically irregular three-story building was tested on this brand-new shaking table. From the simulation of the test results and further analyses through the validated numerical model, the summary and conclusions of this study are as follows:

1. Even though simple beam-column elements allowing concentrated plasticity simulated as plastic hinges at the two ends of each element were adopted in the numerical model, satisfactory simulation was achieved. The key factors of successfully modeling the three-story building lie on the effective section rigidities and the hysteretic loops of the RC columns and beams. The common practice, which simply uses $0.2E_cI_g$ for all beams and columns, results in over twofold errors of the estimated peak inter-story drift as compared with the validated numerical model.
2. The incipient intensities of the scaled ground motions causing the collapse of the three-story building were estimated by means of the incremental dynamic analysis method. It is natural to find that the numerical model is eventually collapsed as a result of the collapse mechanism formed at the soft-and-weak first story. In light of the estimated incipient intensities of ground motions causing the building collapse, the near-fault ground motion TCU052 clearly poses more severe threats on the three-story building than the far-field ground motion CHY047.
3. The "structural resurrection" phenomena observed from the IDA curves accompany the decrease of the story shears. In addition, the "structural resurrection" phenomena signal a significant transition of the point in time when the peak displacement of the numerical model occurs. The "structural resurrection" phenomenon is not observable from the static pushover analysis. Furthermore, the "structural resurrection" indicates that not only the extent but also the distribution of structural damage in buildings subjected to scaled ground motion records may be substantially different from those obtained from the original ground motion records.

4. The collapse of the numerical model under the shaking of the near-fault ground motion TCU052 is characterized by a two-side spike in the building's displacement response history. In addition, the magnitudes of the spikes on the two sides (i.e. the positive and negative displacements) are very close. In contrast, there is no such characterization when the numerical model is collapsed under the shaking of the far-field ground motion CHY047. The two-sided spike phenomenon found here, which is limited to the selected one near-fault ground motion, may be related to the characteristics of the vertically irregular building and/or the ground motion record. The conditions under which the two-side spike occurs and the influence of the two-side spike on buildings' collapse require further study.

With the advanced facilities in the NCREE Tainan lab, comprehensive studies associated with near-fault ground motions will be devotedly performed in cooperation with earthquake engineering communities around the world.

Declaration of conflicting interests

The author(s) declared no potential conflicts of interest with respect to the research, authorship, and/or publication of this article.

Funding

The author(s) disclosed receipt of the following financial support for the research, authorship, and/or publication of this article: The authors gratefully acknowledge the financial support given by the Ministry of Science and Technology, R.O.C. to this research under grant MOST 108-2221-E-492-002. This research was also sponsored in part by the National Applied Research Laboratories, Taiwan, R.O.C. through the Shakeout Project. Special thanks are given to many other colleagues whose efforts, put together, accomplished this shaking table test and the component test.

References

ACI Committee 318 (2008) *Building Code Requirements for Structural Concrete (ACI 318-08) and Commentary*. Farmington Hills, MI: American Concrete Institute.

Alavi B and Krawinkler H (2004) Behavior of moment-resisting frame structures subjected to near-fault ground motions. *Earthquake Engineering and Structural Dynamics* 33: 687–706.

American Society of Civil Engineers (ASCE) (2000) *Prestandard and Commentary for the Seismic Rehabilitation of Buildings, FEMA 356*. Washington, DC: FEMA.

American Society of Civil Engineers (ASCE) (2010) *Minimum Design Loads for Buildings and Other Structures, ASCE/SEI 7–10*. Reston, VA: ASCE.

Baltzopoulos G, Vamvatisikos D and Iervolino I (2016) Analytical modeling of near-source pulse-like seismic demand for multi-linear backbone oscillators. *Earthquake Engineering and Structural Dynamics* 45: 1797–1815.

Chintanapakdee C and Chopra AK (2004) Seismic response of vertically irregular frames: Response history and modal pushover analyses. *Journal of Structural Engineering* 130: 1177–1185.

Chiou TC, Weng PW, Shen WC, Ho YS, Hwang SJ and Chung LL (2018) *Damaged Building Data of the 2016 Meinong Earthquake in Tainan City, NCREE-18-004*. Taipei, Taiwan: National Center for Research on Earthquake Engineering (in Chinese).

Chopra AK and Chintanapakdee C (2001) Comparing response of SDF systems to near-fault and far-fault earthquake motions in the context of spectral regions. *Earthquake Engineering and Structural Dynamics* 30: 1769–1789.

Chopra AK and Goel RK (2002) A modal pushover analysis procedure for estimating seismic demands for buildings. *Earthquake Engineering and Structural Dynamics* 31: 561–582.

Construction and Planning Agency, Ministry of the Interior (CPAMI) (1989) *Building Technical Regulations*. Taipei, Taiwan: CPAMI (in Chinese).

Construction and Planning Agency, Ministry of the Interior (CPAMI) (2011) *Seismic Design Provisions and Commentary for Buildings*. Taipei, Taiwan: CPAMI (in Chinese).

Elwood KJ and Eberhard MO (2006) Effective stiffness of reinforced concrete columns. *PEER Research Digest* 2006-1: 1–5.

Federal Emergency Management Agency (FEMA) (2009) *Quantification of Building Seismic Performance Factors, FEMA Report P695* (ATC for the Federal Emergency Management Agency). Washington, DC: FEMA.

Gibbings JC (2011) *Dimensional Analysis*. London: Springer-Verlag.

Ibarra LF, Medina RA and Krawinkler H (2005) Hysteretic models that incorporate strength and stiffness deterioration. *Earthquake Engineering and Structural Dynamics* 34: 1489–1511.

Lin BZ, Chuang MC and Tsai KC (2009) Object-oriented development and application of a nonlinear structural analysis framework. *Advances in Engineering Software* 40: 66–82.

Michalis F, Dimitrios V and Manolis P (2006) Evaluation of the influence of vertical irregularities on the seismic performance of a nine-storey steel frame. *Earthquake Engineering and Structural Dynamics* 35: 1489–1509.

Moehle JP and Alarcon LF (1986) Seismic analysis methods for irregular buildings. *Journal of Structural Engineering* 112: 35–52.

Panagiotakos TB and Fardis MN (2001) Deformation of reinforced concrete members at yielding and ultimate. *ACI Structural Journal* 98: 135–148.

Park YJ and Ang AHS (1985) Mechanistic seismic damage model for reinforced concrete. *Journal of Structural Engineering* 111: 722–739.

Soni DP and Mistry BB (2006) Qualitative review of seismic response of vertically irregular building frames. *ISET Journal of Earthquake Technology, Technical Note* 43: 121–132.

Spacone E, Filippou FC and Taucer FF (1996) Fiber beam-column model for non-linear analysis of R/C frames: Part I. Formulation. *Earthquake Engineering and Structural Dynamics* 25: 711–725.

Tsai KC and Lin BZ (2003) *Development of an object-oriented nonlinear static and dynamic 3D structural analysis program*. Report no. CEER-92-04. Taipei, Taiwan: Center for Earthquake Engineering Research, National Taiwan University (in Chinese).

Uniform Building Code (UBC) (1994) Whittier, CA: International Conference of Building Officials.

Valmundsson EV and Nau JM (1997) Seismic response of building frames with vertical structural irregularities. *Journal of Structural Engineering* 123: 30–41.

Vamvatisikos D and Cornell CA (2002) Incremental dynamic analysis. *Earthquake Engineering and Structural Dynamics* 31: 491–514.

Vamvatisikos D and Cornell CA (2004) Applied incremental dynamic analysis. *Earthquake Spectra* 20: 523–533.